Modelling of coupled cross-flow and in-line vortex-induced vibrations of flexible cylindrical structures. Part I

model description and validation

Qu, Yang; Metrikine, Andrei V.

DOI
10.1007/s11071-020-06168-3

Publication date
2021

Document Version
Accepted author manuscript

Published in
Nonlinear Dynamics

Noname manuscript No.
(will be inserted by the editor)

Modelling of coupled cross-flow and in-line vortex-induced vibrations of flexible cylindrical structures. Part I: Model description and validation

Yang Qu · Andrei V. Metrikine

Received: date / Accepted: date

Abstract This paper is first of the two papers dealing with the nonlinear modelling and investigation of coupled cross-flow and in-line vortex-induced vibrations (VIVs) of flexible cylindrical structures. As a continuation of the previous work [1] where a new single wake oscillator model was proposed and studied for VIVs of rigid cylinders, the present paper focuses on applying it to flexible cylinders. In this paper, the structure is modelled as an extensible Euler-Bernoulli beam and its 3D nonlinear coupling motion is described in the absolute coordinate system. The single van der Pol wake oscillator model with nonlinear coupling to the in-line motion of the structure, in addition to the classic linear cross-flow motion coupling, is uniformly distributed along the structure to model the hydrodynamic force acting on it. The finite element method has been applied to solve the dynamics of the coupled system, and the experiments of the VIV of a top-tensioned straight riser subjected to a step flow have been taken for the validation of the model. The model has been shown to be able to capture most features of VIVs of flexible cylinders, and a good agreement between the simulation results and the experimental measurements has been observed with regard to the amplitude, frequency and excited mode of both cross-flow and in-line vibrations, as well as the mean in-line deflection due to the amplified in-line force. While it is conventionally expected that the VIV of a flexible cylinder subjected to a uniform flow is dominated by a single frequency, a multi-frequency response is observed in the simulation results over the range of flow velocities through which the transition of the dominant mode of vibration occurs.

Keywords Vortex-induced vibration · In-line coupling · Wake oscillator · Fluid-structure interaction

Y. Qu (Corresponding author) and A.V. Metrikine
Department of Hydraulic Engineering, Delft University of Technology, Stevinweg 1, 2628CN Delft, The Netherlands

Present address of Y. Qu
State Key Laboratory of Ocean Engineering, Shanghai Jiao Tong University, Shanghai, 200240, China
E-mail: yangqu@sjtu.edu.cn

1 Introduction

Vortex-induced vibration (VIV) is a well-known phenomenon related to civil engineering structures, such as chimneys, cables of suspended bridges, suspended power lines, offshore risers and mooring cables, that are subjected to air or water flows. VIVs of flexible structures are important sources of fatigue damage, and the reliable prediction thereof has been a long-standing problem.

In most studies of VIVs of flexible cylinders, the focus has been placed on the analysis and prediction of the vibration of a top-tensioned riser, which can be adequately modelled as a tensioned beam or cable with appropriate boundary conditions. With a small amplitude of vibration, the structural dynamics model is normally assumed to be linear, and the cross-flow and in-line motions are considered separately [2–5]. However, in practical applications, many long, slender structures, such as catenary risers, pipelines during laying processes and mooring cables, have a curved shape. Due to the high slenderness of the structure and complicated environmental loads, the dynamics of these structures often exhibit strong 3D nonlinear coupling motions. Therefore, a general, realistic, nonlinear model of the structure that is valid for both straight and curved structures is needed. To authors' knowledge, only a few works have

considered such structural nonlinearities in the study of VIV [6–8].

The main difficulty related to the reliable prediction of VIV lies in the modelling of hydrodynamic forces. As solving the equations governing the viscous flow that interacts with the structure is extremely computationally demanding, the industry relies mainly on the force-decomposition method for the prediction of VIVs of flexible structures. This method, originally based on the work by Sarpkaya [9], is semi-empirical. The basis of the method is the use of a hydrodynamic forces database, which is obtained from forced vibration tests [10–12]. Based on this method, several frequency domain tools, such as VIVANA and SHEAR7, have been developed and widely used by the industry. More recently, a unique modal space direct VIV prediction method has been developed and validated by Lu et.al [13]. This new method converts the VIV prediction problem into modal space and solves the equations by graphically finding their crossing point of two curves of modal response and modal hydrodynamic force without any numerical iterations and calculation of energies. Despite of its wide applications, the force decomposition method is a frequency domain approach and is not able to consider the nonlinear structural behaviours. Moreover, a hydrodynamic database that takes both cross-flow and in-line motions into account is required for this method to be applied in the prediction of coupled cross-flow and in-line VIVs. An attempt has been made to conduct two degrees of freedom (2DOF) forced vibrations to build such an advanced force database. However, the large number of control parameters makes it difficult to build a complete database with sufficient resolution, and interpolating the relatively sparse database is not an ideal option due to the strong nonlinearity of the problem [14].

The wake oscillator model is another type of model that is more often used in the research field than in the industry for the prediction of VIV. The fundamental idea of this approach is to describe the dynamics of the wake using an effective nonlinear oscillator, whose motion is coupled to the dynamics of the cylinder. Since the first proposal of the concept in the 1950s, a large number of wake oscillators have been developed; for details of these models please refer to [15]. In general, the van der Pol type nonlinear oscillators have been mostly used and this type of nonlinear oscillators describes the hydrodynamic forces acting on a fixed cylinder better than others, e.g., Rayleigh type nonlinear oscillators [16]. Studies have revealed that the wake oscillator models are capable of capturing key VIV features in qualitative, sometimes quantitative, agreement with experimental observations and direct numerical simulations for both rigid and flexible cylinders [2,17,18]. There are also progresses in the derivation of reduced-order model of VIV from first principles, which have provided more insight into the underlying physics and hydrodynamic basis of the wake oscillator model [19, 20].

Apart from the methods described above, other models have also been developed - for detailed information, please refer to the review by Gabbai et al. [15]. Developing new time domain models for VIVs of flexible cylinders subjected to both steady and oscillatory flows has been the focus of many recent studies [21–23]. Especially, Zhang et. al [22] proposed an empirical time domain prediction method where for the first-time couplings between tension variations and VIV were considered via a simplified tension variation model. This new method provides the possibility to evaluate effects of tension variations on VIVs, becoming an indispensable reference to VIV researches.

In most studies on wake oscillator models, only the cross-flow VIV is considered and the in-line response is normally assumed to be very small and its influence is ignored. However, experimental studies have demonstrated that the presence of the in-line vibration can alter the wake pattern, and the VIV of a rigid cylinder free to move in both cross-flow and in-line directions can be significantly different from the case where the cylinder is constrained to move in only one direction [24–26]. With regard to this problem, a few double wake oscillator models have been developed; a second wake oscillator equation is introduced in the model to describe the fluctuating drag force [27–29]. However, introducing a second oscillator equation to describe the fluctuating drag force seems to contradict the fundamental mechanism of the coupled cross-flow and in-line VIV where the lift and drag forces have the same origin, i.e., the dynamics of the wake. It is physically more reasonable to use only one oscillator to describe the dynamics of the wake, and this oscillator should be coupled to both cross-flow and in-line motions of the cylinder.

In line with this principle, a single van der Pol wake oscillator model has been developed in [1]. In addition to the classic linear cross-flow acceleration coupling as suggested in [17], a nonlinear in-line coupling term has been introduced to the wake oscillator equation. This new model overcomes the main limitations of the double wake oscillator models and has been shown to be able to reproduce important features of coupled cross-flow and in-line VIVs of rigid cylinders that the double wake oscillator models have failed to capture [1]. With the previous paper [1] focusing on rigid cylinders, the main purpose of the present work is to investigate how this new wake oscillator model performs with respec-

t to predicting coupled cross-flow and in-line VIVs of flexible cylinders. As the VIVs of flexible cylinders are significantly different from and more complicated than those of rigid cylinders, the effect of the in-line coupling which has been studied to some extent in [1] for rigid cylinders needs to be evaluated from different perspectives, such as the response pattern, force distribution, energy transfer and fatigue damage. Due to its extensive content, the work is presented in two parts. The first part is related to the model description and validation which is the focus of the present paper, while the second part is presented in another (Part II) where the effect of the in-line coupling as well as its importance on the prediction of coupled cross-flow and in-line VIVs of flexible cylinders are thoroughly discussed.

The remainder of the paper is structured as follows. In Section 2, the models of both the structure and hydrodynamic force are described. The models are then applied to simulate the experiments presented in [30], and the comparison between the results of the simulations and experiments are discussed in Section 3. Finally, the main conclusions are presented in Section 4.

2 Model description

In this section, the structural and hydrodynamic force models for the simulation of VIVs of flexible cylinders are described. The structure is modelled as an extensible Euler-Bernoulli beam, which can deal with both straight and curved configurations, and a three dimensional nonlinear coupled motion is considered. A local reference frame is introduced at each location along the cylinder within which the wake oscillator model in [1] is applied to model the hydrodynamic force.

2.1 Nonlinear structural model

The flexible cylinder is simplified into a beam. In line with the Euler-Bernoulli beam theory, only the axial and bending deformations are considered. This is a reasonable simplification in most cases when the shear deformation and torsion are negligible, and it is computationally more efficient. The configuration of the structure is described by the position vector $\mathbf{r}(p,t)$ of the cylinder axis as

$$\mathbf{r}(p,t) = \begin{bmatrix} x(p,t) \\ y(p,t) \\ z(p,t) \end{bmatrix} \tag{1}$$

where p is the Lagrange coordinate or arc-length measured along the undeformed cylinder, and t is the time. For the convenience of writing, the following notation will be used to represent the partial derivative with respect to p: $\mathbf{r}_{,p} = \partial\mathbf{r}/\partial p$ and overdots represent the derivative with respect to time.

The weak form of the equation of motion is given as

$$\delta W_I + \delta W_S - \delta W_E = 0 \tag{2}$$

where δW_I denotes the virtual work of inertia forces, δW_S is the virtual work of internal (elastic) forces, and δW_E is the virtual work of external forces.

The expressions of virtual work of inertia force is given as

$$\delta W_I = \int_0^L m_0 \ddot{\mathbf{r}}^T \delta\mathbf{r} dp \tag{3}$$

where L is the length of undeformed beam and m_0 is the mass of the beam per unit length.

The virtual work of internal forces, as proposed in [31], is divided into two parts: one due to the bending moment and another due to the axial force. That virtual work reads as follows:

$$\delta W_S = \int_0^L \left(EA\epsilon_0\delta\epsilon_0 + EIK\delta K\right) dp \tag{4}$$

in which E is the modulus of elasticity, A is the cross-sectional area and I is the second moment of the area. Furthermore, ϵ_0 is the axial strain, which is defined as

$$\epsilon_0 = |\mathbf{r}_{,p}| - 1 \tag{5}$$

and K, interpreted in [32] as the *material measure of curvature*, is defined as

$$K = \frac{|\mathbf{r}_{,p} \times \mathbf{r}_{,pp}|}{|\mathbf{r}_{,p}|^2} \tag{6}$$

The variation of axial strain ϵ_0 is given by

$$\delta\epsilon_0 = \frac{1}{|\mathbf{r}_{,p}|}\mathbf{r}_{,p}^{\intercal}\delta\mathbf{r}_{,p} \tag{7}$$

The variation of K reads

$$\begin{aligned}\delta K = &-2\frac{|\mathbf{r}_{,p} \times \mathbf{r}_{,pp}|}{|\mathbf{r}_{,p}|^4}\mathbf{r}_{,p}^T\delta\mathbf{r}_{,p} \\ &+\frac{1}{|\mathbf{r}_{,p}|^2|\mathbf{r}_{,p} \times \mathbf{r}_{,pp}|}\left(\mathbf{r}_{,p} \times \mathbf{r}_{,pp}\right)^{\intercal}\left(\delta\mathbf{r}_{,p} \times \mathbf{r}_{,pp} + \mathbf{r}_{,p} \times \delta\mathbf{r}_{,pp}\right)\end{aligned} \tag{8}$$

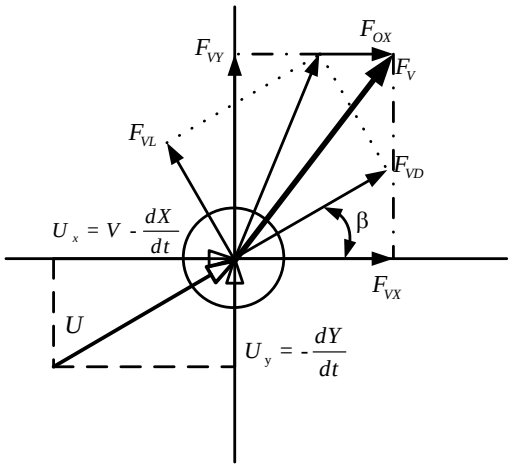

Fig. 1: Decomposition of the vortex force in drag, lift, cross-flow and in-line directions

2.2 Hydrodynamic force model

In this study, the single van der Pol wake oscillator model proposed in [1] for rigid cylinders is now applied and distributed along the structure to compute the hydrodynamic forces due to vortex shedding at each cross section. In order to introduce the model, we consider a case where the cylinder is rigid and the flow, with velocity V, is perpendicular to its axis. By assuming that the flow around the cylinder is two-dimensional (uniform along the cylinder axis), the interaction between the cylinder and the flow can be simplified as shown in Fig.1 .Taking into account of the relative flow velocity (U) between the free stream flow and the two-DOF moving cylinder, the instantaneous lift (F_{VL}) and drag (F_{VD}) forces acting on the cylinder are assumed to be perpendicular to and aligned with U, respectively.

The magnitudes of lift and drag forces per unit length are related to the relative flow velocity U and are defined as

$$F_{VL} = \frac{1}{2}\rho D U^2 C_{VL}, \quad F_{VD} = \frac{1}{2}\rho D U^2 C_{VD} \tag{9}$$

where ρ is the mass density of the fluid, D is the diameter of the cylinder, C_{VL} and C_{VD} are lift and drag force coefficients respectively, the relative flow velocity is expressed as

$$U = \sqrt{\left(V - \frac{\mathrm{d}X}{\mathrm{d}t}\right)^2 + \left(\frac{\mathrm{d}Y}{\mathrm{d}t}\right)^2} \tag{10}$$

In Eq.(9), the drag coefficient C_{VD} is assumed to be constant and the influence of the dynamics of the wake is taken into account through time varying lift coefficient C_{VL}. One major problem with this force formulation is that it ignores the oscillatory component of the drag force. Therefore, an additional in-line force F_{OX} is introduced which is given as

$$F_{OX} = \frac{1}{2}\alpha C_{VL}^2 \rho D |U_x| U_x, \tag{11}$$

where α is an empirical parameter and $U_x = V - \mathrm{d}X/\mathrm{d}t$ is the relative flow velocity in the in-line direction. Physically, the lift and drag forces are projections of the total fluid force in different directions and the two forces are therefore interdependent. To account for this interdependency, the quadratic drag-lift coupling as shown in Eq.(11) is adopted according to the work [33] where the frequency components and phase relation of the lift and drag forces are studied using higher-order spectral moments.

The cross-flow (F_{VY}) and in-line (F_{VX}) hydrodynamic forces can be obtained, by projecting the F_{VD} and F_{VL} components onto the cross-flow and in-line axes, as

$$F_{VY} = F_{VD}\sin\beta + F_{VL}\cos\beta \tag{12}$$

$$F_{VX} = F_{VD}\cos\beta - F_{VL}\sin\beta + F_{OX} \tag{13}$$

where β is the angle between the direction of the relative flow velocity U and the undisturbed flow V. The angle β is given by

$$\sin(\beta) = -\frac{\mathrm{d}Y}{\mathrm{d}t}/U, \quad \cos(\beta) = (V - \frac{\mathrm{d}X}{\mathrm{d}t})/U \tag{14}$$

Substituting Eqs.(9, 10, 11) and (14) into Eqs.(12) and (13), we obtain

$$F_{VY} = \frac{1}{2}\rho D V^2 C_{VY} \tag{15}$$

$$F_{VX} = \frac{1}{2}\rho D V^2 C_{VX} \tag{16}$$

where

$$C_{VY} = C_{VL}\frac{U}{V^2}\left(V - \frac{\mathrm{d}X}{\mathrm{d}t}\right) - C_{VD}\frac{U}{V^2}\frac{\mathrm{d}Y}{\mathrm{d}t} \tag{17}$$

$$\begin{aligned} C_{VX} =& C_{VL}\frac{U}{V^2}\frac{\mathrm{d}Y}{\mathrm{d}t} + C_{VD}\frac{U}{V^2}\left(V - \frac{\mathrm{d}X}{\mathrm{d}t}\right) \\ &+ \alpha C_{VL}^2\left(1 - \frac{1}{V}\frac{\mathrm{d}X}{\mathrm{d}t}\right)\left|1 - \frac{1}{V}\frac{\mathrm{d}X}{\mathrm{d}t}\right| \end{aligned} \tag{18}$$

When a cylinder does not move, i.e. $\mathrm{d}X/\mathrm{d}t = 0$ and $\mathrm{d}Y/\mathrm{d}t = 0$, Eq.(18) reduces to

$$C_{VX} = C_{VD} + \alpha C_{VL}^2 \tag{19}$$

which is in the same form as proposed by Qin [33] for the coupled lift and drag forces on a fixed cylinder. If the lift force acting on a fixed cylinder is expressed

as $C_{VL} = C_{L0}\sin(\omega t)$, where C_{L0} is the amplitude of fluctuating lift force coefficient. Then, substituting it into Eq.(19) results in

$$C_{VX} = C_{VD} + \frac{1}{2}\alpha C_{L0}^2\left(1-\cos(2\omega t)\right) \tag{20}$$

The mean value of C_{VX} is $C_{VD} + \frac{1}{2}\alpha C_{L0}^2$ and the amplitude of the fluctuating component of C_{VX} is $\frac{1}{2}\alpha C_{L0}^2$, as can be derived from Eq.(20). Comparing the mean and fluctuating components of C_{VX} to those measured on a fixed cylinder, the values of C_{VD} and α can be obtained as

$$C_{VD} = \overline{C}_D - \frac{1}{2}\alpha C_{L0}^2 \tag{21}$$

and

$$\alpha = 2\frac{C_{D0}}{C_{L0}^2} \tag{22}$$

where $\overline{C}_D$ is the mean drag force coefficient and C_{D0} is the amplitude of the fluctuating drag force coefficient measured on a fixed cylinder.

The dynamics of the wake is modelled by a van der Pol nonlinear equation which is coupled to both the cross-flow and in-line motions of the cylinder. The equation is given as

$$\frac{\mathrm{d}^2 q}{\mathrm{d}t^2} + \epsilon\omega_s(q^2-1)\frac{\mathrm{d}q}{dt} + \omega_s^2 q - \kappa\frac{\omega_s^4 D\frac{\mathrm{d}^2 X}{\mathrm{d}t^2}}{\omega_s^4 D^2 + \left(\frac{\mathrm{d}^2 X}{\mathrm{d}t^2}\right)^2}q = \frac{A}{D}\frac{\mathrm{d}^2 Y}{\mathrm{d}t^2} \tag{23}$$

where q is the wake variable; ϵ, A and κ are tuning parameters; $\omega_s = 2\pi V\mathrm{St}/D$ is the Strouhal frequency and St is the Strouhal number. Compared with the conventional wake oscillator equation for the cross-flow VIV, Eq.(23) introduces a nonlinear in-line coupling term to describe the influence of the in-line motion on the dynamics of the wake. This relatively complicated in-line coupling term is the result of modifying a simpler form of parametric excitation $\frac{\kappa}{D}\frac{\mathrm{d}^2 X}{\mathrm{d}t^2}q$, which was derived based on the experimental observation and heuristic inference from the dynamics of a pendulum, to overcome its limitation when subjected to forced in-line vibrations at high frequencies [1]. It needs to be clarified that Qu and Metrikine [1] were not the first to propose introducing in-line coupling in the form of parametric excitation. This idea has been suggested before in the work by Qin [33].

The lift force coefficient C_{VL} is associated with the wake variable q as

$$C_{VL} = \frac{q}{2}C_{L0} \tag{24}$$

With $X = 0$ and $Y = 0$, Eq.(23) describes the lift force that wake imposes on a fixed cylinder. In such case, the steady solution of Eq.(23) reaches a limit cycle with the amplitude of 2. Therefore, the coefficient $1/2$ in Eq.(24) is used to ensure the amplitude of oscillation of C_{VL} equals to C_{L0} for a fixed cylinder.

Choosing appropriate tuning parameters is important in the application of the wake oscillator model to simulate VIVs of flexible cylinders. A common practise is to use the tuning parameters that have been calibrated against experiments of rigid cylinders by assuming that the flow field around a flexible cylinder at each local cross section is the same as that around a rigid one [2,5,8]. The same approach is adopted here. However, in the work [1] where the present wake oscillator model is tuned to experiments of rigid cylinders, two different sets of values for tuning parameters A, ϵ and κ have been applied to capture the upper and lower response branches respectively. It is not clear yet which set of values should be used here for flexible cylinders. A flexible cylinder possesses infinite number of natural frequencies, and the cross-flow and in-line vibrations of it are normally characterized by dual resonance when VIV occurs [34]; this is more similar to the case of a rigid cylinder with the in-line natural frequency approximately twice that of the cross-flow. As the ratio between the in-line and cross-flow natural frequencies increases from 1 to 2, it was observed in experiments that the cross-flow response becomes dominated by one response branch over a wide range of reduced velocities and this response branch exhibits two distinct peaks [35]. A preliminary study indicates that the current model qualitatively captures this characteristic using the set of tuning parameters of Case U given in [1]; see Appendix A. Therefore, these tuning parameters, namely $A = 8$, $\epsilon = 0.08$ and $\kappa = 5$, will be applied in the following for the modelling of VIVs of flexible cylinders.

2.3 Coupled system

As mentioned in the previous paragraphs, the wake oscillator model described above is developed for rigid cylinders subjected to the normal uniform cross flow. However, in many engineering applications of long, flexible cylinders, the flow may not be uniform (shear flow) and, in many cases, not perpendicular to the axis of the cylinder, such as in the case of a catenary riser. In such cases, the independence principle is normally applied; it assumes that the flow dynamics are essentially dependent on the normal component of free stream with respect to the cylinder axis, while the component that

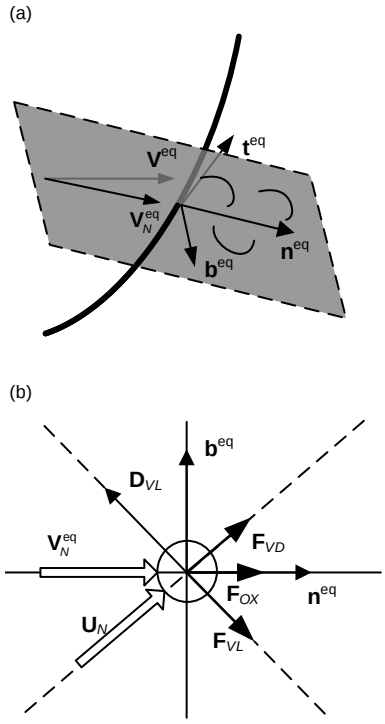

Fig. 2: Local vortex shedding for a curved beam and definition of the local coordinate system: (a) local coordinate system and (b) force decomposition in plane $\mathbf{b}^{eq} - \mathbf{n}^{eq}$.

is aligned with the cylinder axis has a negligible impact. Here, the inclination angle is defined as the angle between the incoming flow and the plane that is perpendicular to the cylinder axis.

To apply the wake oscillator for the modelling of VIVs of flexible cylinders, a local coordinate must first be established at each cross-section. Since the VIV of a flexible structure is normally characterised as finite amplitude motions around the equilibrium position, it is reasonable to build up the local coordinate system based on the equilibrium position of the structure. Consider a segment of a cylinder at its equilibrium position subjected to the flow, as illustrated in Fig.2(a). Using the local frame described by the tangential unit vector $\mathbf{t}^{eq}$, in-line unit vector $\mathbf{n}^{eq}$ and cross-flow unit vector $\mathbf{b}^{eq}$, according to the independence principle, the vortex shedding process is assumed to take place in the plane that is perpendicular to the orientation of the beam, i.e., the $\mathbf{b}^{eq} - \mathbf{n}^{eq}$ plane. Here, the superscript 'eq' signifies that the vectors are obtained in the equilibrium position. According to [36], the tangential unit vector $\mathbf{t}^{eq}$ is given as

$$\mathbf{t}^{eq} = \frac{\mathbf{r}_{,p}^{eq}}{|\mathbf{r}_{,p}^{eq}|}. \tag{25}$$

Under the equilibrium configuration, the free stream velocity at a specific location of the structure is $\mathbf{V}^{eq}$, and its component within the plane of vortex shedding, i.e., $\mathbf{b}^{eq} - \mathbf{n}^{eq}$, is obtained as

$$\mathbf{V}_N^{eq} = \mathbf{V}^{eq} - ((\mathbf{V}^{eq})^\intercal \mathbf{t}^{eq})\, \mathbf{t}^{eq}. \tag{26}$$

where $[]^\intercal$ denotes transpose operator.

The in-line unit vector $\mathbf{n}^{eq}$ is defined to be in the same direction as $\mathbf{V}_N^{eq}$, and it reads

$$\mathbf{n}^{eq} = \frac{\mathbf{V}_N^{eq}}{|\mathbf{V}_N^{eq}|}. \tag{27}$$

The cross-flow unit vector $\mathbf{b}^{eq}$ is defined as the following cross product:

$$\mathbf{b}^{eq} = \mathbf{t}^{eq} \times \mathbf{n}^{eq}. \tag{28}$$

The unit vectors $\mathbf{t}^{eq}$, $\mathbf{n}^{eq}$ and $\mathbf{b}^{eq}$ formulate the local coordinate system within which the wake oscillator described in Section 2.2 is applied. The unit vector $\mathbf{b}^{eq}$ corresponds to the cross-flow direction of the rigid cylinder, and the unit vector $\mathbf{n}^{eq}$ corresponds to the in-line direction. Within the plane $\mathbf{b}^{eq} - \mathbf{n}^{eq}$, the force decomposition is the same as that for a rigid cylinder and is depicted in Fig.2(b). It has to be pointed out that this local coordinate system is based on the equilibrium configuration of the structure and does not change as the structure vibrates. The same rule applies to the corresponding parameters (with the superscript 'eq') that are derived from the equilibrium position. Within the local coordinate, the wake oscillator equation can be written as

$$\ddot{q} + \omega_s \left(q^2 - 1\right) \dot{q} + \omega_s^2 q - \kappa \frac{\omega_s^4 D \ddot{\mathbf{r}}^\intercal \mathbf{n}^{eq}}{\omega_s^4 D^2 + \left(\ddot{\mathbf{r}}^\intercal \mathbf{n}^{eq}\right)^2} q = \frac{A}{D} \ddot{\mathbf{r}}^\intercal \mathbf{b}^{eq} \tag{29}$$

where $\omega_s = 2\pi \mathrm{St} |\mathbf{V}_N^{eq}| / D$. The instantaneous lift and drag forces per unit length are defined as

$$\mathbf{F}_{VL} = \frac{1}{2} \rho D \frac{C_{L0}}{2} q |\mathbf{U}_N|^2 \mathbf{D}_{VL} \tag{30}$$

$$\mathbf{F}_{VD} = \frac{1}{2} \rho D C_{VD} |\mathbf{U}_N| \mathbf{U}_N \tag{31}$$

where $\mathbf{U}_N$ is the relative flow velocity within plane $\mathbf{b}^{eq} - \mathbf{n}^{eq}$, which is given as

$$\mathbf{U}_N = \mathbf{V}_N^{eq} - (\dot{\mathbf{r}} - (\dot{\mathbf{r}}^\intercal \mathbf{t}^{eq})\, \mathbf{t}^{eq}) \tag{32}$$

and $\mathbf{D}_{VL}$ is the unit vector in the **b**-**n** plane that is perpendicular to $\mathbf{U}_N$ and is given as

$$\mathbf{D}_{VL} = \frac{\mathbf{t}^{eq} \times \mathbf{U}_N}{|\mathbf{t}^{eq} \times \mathbf{U}_N|}. \tag{33}$$

The extra in-line oscillating force, denoted by $\mathbf{F}_{OX}$ is given as

$$\mathbf{F}_{OX} = \frac{1}{2}\rho D\alpha \frac{C_{L0}^2}{4} q^2 |\mathbf{U}_{NX}| \mathbf{U}_{NX} \tag{34}$$

where

$$\mathbf{U}_{NX} = \mathbf{V}_N^{\mathrm{eq}} - \left((\mathbf{n}^{\mathrm{eq}})^{\intercal}\, \dot{\mathbf{r}}\right) \mathbf{n}^{\mathrm{eq}}. \tag{35}$$

Apart from the hydrodynamic force, the structure is also subjected to a hydrostatic force when submerged in the fluid. The concept of effective tension is normally used in offshore engineering to take into account the effect of hydrostatic fluid pressure. The effective tension approach states that the total effect of the structure's fluid pressure, internal or external, on a section of the structure can be replaced by the buoyancy force that follows the Archimedes' principle and an axial tension equal to $P_e A_e - P_i A_i$, where P_e is the external fluid pressure, A_e is the corresponding external area of the cross-section, P_i is the internal fluid pressure, and A_i is the corresponding internal area of the cross-section. The buoyancy force is treated as the external distributed force, while the tension $P_e A_e - P_i A_i$ will be taken as the internal force and incorporated into the equation of motion of the structure. For simplicity, here the $P_e A_e - P_i A_i$ is calculated based on the equilibrium configuration of the structure and does not change during the vibration. Another effect of the fluid on the motion of the structure that has not been addressed in the previous paragraphs is the potential inertial force (potential added mass). This force should be considered as acting in the direction normal to the cylinder axis and proportional to the acceleration of the structure in that direction. For simplicity, we also assume that this direction is defined in the equilibrium configuration of the structure and does not change during the vibration. This enables us to integrate the potential added mass into the mass matrix of the structure and added mass coefficient $C_a = 1$ is taken.

2.4 Finite element formulation

Fig.3 depicts a two-noded beam element, which is the same as the lower-order element proposed by Gerstmayr et al. [31], with two nodes A and B at each end. Each node is defined by six degrees of freedom that consist of the nodal global position vector and slope vector:

$$\mathbf{u}_j = \begin{bmatrix} \mathbf{r}_j^{\intercal} & \mathbf{r}_{j,p}^{\intercal} \end{bmatrix}^{\intercal} \quad j = A, B. \tag{36}$$

Then, the beam element coordinates are given by the vector

$$\mathbf{u} = \begin{bmatrix} \mathbf{u}_A^{\intercal} & \mathbf{u}_B^{\intercal} \end{bmatrix}^{\intercal}. \tag{37}$$

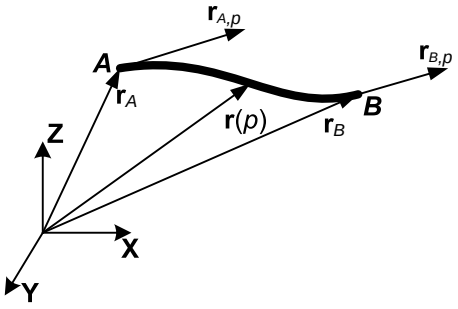

Fig. 3: Two-noded beam element.

The global position vector of an arbitrary point within the beam element, originally placed at p of the undeformed beam axis, in the deformed configuration can be interpolated in terms of the nodal coordinates and the element shape function as

$$\mathbf{r}(p,t) = \begin{bmatrix} x(p,t) \\ y(p,t) \\ z(p,t) \end{bmatrix} = \mathbf{S}\mathbf{u}. \tag{38}$$

Hermite shape functions are employed, and the shape function matrix S is written as

$$\mathbf{S} = [S_1\mathbf{I} \quad S_2\mathbf{I} \quad S_3\mathbf{I} \quad S_4\mathbf{I}] \tag{39}$$

where $\mathbf{I}$ is the 3×3 unit matrix, and functions $S_i = S_i(p)$ are given by

$$\begin{aligned} S_1 &= 2\left(\frac{p}{L}\right)^3 - 3\left(\frac{p}{L}\right)^2 + 1 \\ S_2 &= L\left(\frac{p}{L}\right)^3 - 2L\left(\frac{p}{L}\right)^2 + p \\ S_3 &= 3\left(\frac{p}{L}\right)^2 - 2\left(\frac{p}{L}\right)^3 \\ S_4 &= L\left(\frac{p}{L}\right)^3 - L\left(\frac{p}{L}\right)^2 \end{aligned} \tag{40}$$

By substituting Eq. (38) into Eq. (3), one obtains the virtual work of inertia force as

$$\delta W_I = \ddot{\mathbf{u}}^{\intercal} \int_0^L m_0 \mathbf{S}^{\intercal}\mathbf{S} dp \delta\mathbf{u} \tag{41}$$

from which the mass matrix of the structure element is determined as

$$\mathbf{M}_s^e = \int_0^L m_0 \mathbf{S}^{\intercal}\mathbf{S} dp \tag{42}$$

Similarly, by substituting Eq.(38) into Eq.(4), the stiffness matrix of the structure element $\mathbf{K}_s^e$ is obtained. The detailed derivation, as well as the final expression of $\mathbf{K}_s^e$, is provided in Appendix B.1.

For the structural damping, the Rayleigh damping model is applied for simplification, and it reads as follows:

$$\mathbf{C}_s^e = \alpha \mathbf{M}_s^e + \beta \mathbf{J}_s^{e,\mathrm{eq}} \tag{43}$$

where $\mathbf{J}_s^{e,\mathrm{eq}} = \frac{\partial[\mathbf{K}^{e,\mathrm{eq}}\mathbf{u}]}{\partial \mathbf{u}}$ is the tangent stiffness matrix calculated under the equilibrium configuration.

The wake oscillators are uniformly distributed along the structure and therefore also need to be discretised in accordance with the beam element. With the same Hermite shape function as that used for the beam element, the wake variable q is interpolated as

$$q\left(p,t\right) = \mathbf{S}_q \mathbf{q} \tag{44}$$

where $\mathbf{q}$ is the wake element coordinates and consists of the wake variable as well as its derivative with respect to p at two nodes of beam element $\mathbf{q} = [q_A \quad q_{A,p} \quad q_B \quad q_{B,p}]^\intercal$. $\mathbf{S}_q$ is the shape function matrix and is written as

$$\mathbf{S}_q = [S_1 \quad S_2 \quad S_3 \quad S_4]. \tag{45}$$

Then, the mass matrix, damping matrix and stiffness matrix of the wake variable element can be obtained from Eq.(29) as

$$\mathbf{M}_q^e = \int_0^L \mathbf{S}_q^\intercal \mathbf{S}_q dp \tag{46}$$

$$\mathbf{C}_q^e = \int_0^L \omega_s \left(\mathbf{q}^\intercal \mathbf{S}_q^\intercal \mathbf{S}_q \mathbf{q} - 1\right) \mathbf{S}_q^\intercal \mathbf{S}_q dp \tag{47}$$

$$\mathbf{K}_q^e = \int_0^L \omega_s^2 \mathbf{S}_q^\intercal \mathbf{S}_q dp - \kappa \int_0^L \frac{\omega_s^4 D\left(\ddot{\mathbf{u}}^\intercal \mathbf{S}^\intercal \mathbf{n}^{\mathrm{eq}}\right)}{\omega_s^4 D^2 + \left(\ddot{\mathbf{u}}^\intercal \mathbf{S}^\intercal \mathbf{n}^{\mathrm{eq}}\right)^2} \mathbf{S}_q^\intercal \mathbf{S}_q dp. \tag{48}$$

By applying the principle of virtual work to Eq.(30), (31) and (34), the nodal hydrodynamic forces are obtained as

$$\begin{aligned} \mathbf{F}^e &= \int_0^L \mathbf{S}^\intercal \left(\mathbf{F}_{VL} + \mathbf{F}_{VD} + \mathbf{F}_{OX}\right) dp \\ &= \frac{1}{2}\rho D \frac{C_{L0}}{2} \int_0^L |\overline{\mathbf{U}}_N|^2 \mathbf{S}^\intercal \overline{\mathbf{D}}_{VL} \mathbf{S}_q \mathbf{q} dp \\ &+ \frac{1}{2}\rho D C_{DM} \int_0^L |\overline{\mathbf{U}}_N| \mathbf{S}^\intercal \overline{\mathbf{U}}_N dp \\ &+ \frac{1}{2}\rho D \alpha \frac{C_{L0}^2}{4} \int_0^L \left(\mathbf{S}_q \mathbf{q}\right)^2 |\overline{\mathbf{U}}_{NX}| \mathbf{S}^\intercal \overline{\mathbf{U}}_{NX} dp \end{aligned} \tag{49}$$

where $\overline{\mathbf{U}}_N$, $\overline{\mathbf{U}}_{NX}$ and $\overline{\mathbf{D}}_{VL}$ are obtained by substituting Eq.(38) into Eqs.(32), (33) and (35) and are given as

$$\overline{\mathbf{U}}_N = V_N^{\mathrm{eq}} - \left(\mathbf{S}\dot{\mathbf{u}} - \left(\dot{\mathbf{u}}^\intercal \mathbf{S}^\intercal \mathbf{t}^{\mathrm{eq}}\right) \mathbf{t}^{\mathrm{eq}}\right) \tag{50}$$

$$\overline{\mathbf{U}}_{NX} = \mathbf{V}_N^{\mathrm{eq}} - \left(\left(\mathbf{n}^{\mathrm{eq}}\right)^\intercal \mathbf{S}\dot{\mathbf{u}}\right) \mathbf{n}^{\mathrm{eq}} \tag{51}$$

$$\overline{\mathbf{D}}_{VL} = \frac{\mathbf{t}^{\mathrm{eq}} \times \overline{\mathbf{U}}_N}{|\mathbf{t}^{\mathrm{eq}} \times \overline{\mathbf{U}}_N|}. \tag{52}$$

Similarly, the external nodal force of the wake oscillator can be obtained as

$$\mathbf{R}^e = \frac{A}{D} \int_0^L \mathbf{S}_q^\intercal \ddot{\mathbf{u}}^\intercal \mathbf{S}^\intercal \mathbf{b}^{\mathrm{eq}} dp. \tag{53}$$

After discretisation, the dynamics of the coupled system are described by ordinary differential equations that, in the matrix form, are given as

$$\mathbf{M}_s^e \ddot{\mathbf{u}} + \mathbf{C}_s^e \dot{\mathbf{u}} + \mathbf{K}_s^e \mathbf{u} = \mathbf{F}^e \tag{54}$$

$$\mathbf{M}_q^e \ddot{\mathbf{q}} + \mathbf{C}_q^e \dot{\mathbf{q}} + \mathbf{K}_q^e \mathbf{q} = \mathbf{R}^e. \tag{55}$$

Implicit Newmark time integration method is used to solve the above equation, and verification of the structural model is also performed, see Appendix **??**-B.4.

3 Model validation against experiments

In this section, the model for VIVs of flexible cylinders that was described in the previous section is used to simulate the experiments conducted by [30], and the simulation results are compared with the experimental measurements.

3.1 Experiment description and coordinate system

In the series of experiments presented in [30] and [37], the cross-flow and in-line vibrations of a vertical tensioned riser were measured when being towed through the still water by a carriage at different speeds. The riser is 13.12 m long, with a diameter of $D = 0.028$ m, and only the lower 45% of its length is submerged in the flume and subjected to a uniform current; the remaining part is in still water. The two ends of the riser are connected to a stiff frame mounted on the carriage through universal joints, and the tension is provided by a set of springs at the top that allows the top end of the riser to move in the vertical direction. The detailed main parameters of the experiment are summarised in Table 1.

To model the experiments, a global Cartesian coordinate system with its origin at the bottom of the riser has been used; see Fig.4. The x-axis is aligned with the flow direction representing the in-line direction; the z-axis coincides with the vertical axis of the riser in its initial configuration, and the y axis is perpendicular to both, representing the cross-flow direction. The riser is pinned to the supporting structure at the bottom, which only allows rotation, while the top of the riser is

Table 1: Properties of the riser model

Parameters	Values	Dimension
External diameter	0.028	m
Length	13.12	m
Aspect ratio	470	-
Submerged Length	5.94	m
Flexural Stiffness	29.88	Nm^2
Mass	1.845	kg/m
Mass ratio	3	-

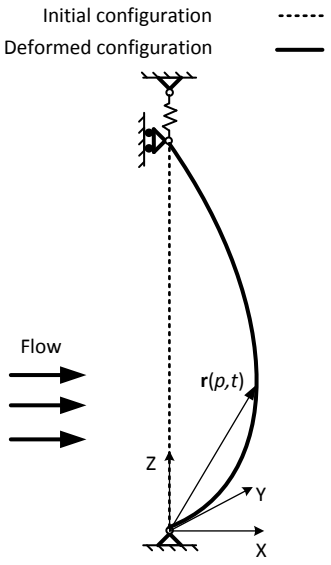

Fig. 4: Schematic of the global coordinate system and riser in its initial and deformed configurations.

pinned to an array of springs hanging from the supporting structure and therefore can move in the z direction. When the riser vibrates, its configuration at any moment is described by the position vector $\mathbf{r}(p,t)$, where p is the coordinate along the riser.

When applying the model described in the previous section, an important part is to determine the equilibrium configuration of the structure, upon which the local coordinate system can be established. However, the mean in-line deflection of the structure, as a result of amplified in-line force, is not known in advance, and an iterative procedure thus is required. Here, for simplicity, the iteration is not included and the local coordinate system at each cross section is established upon the initial vertical configuration of the riser. This is a reasonable simplification since the mean in-line offset of the riser studied in this paper is small compared to its length, i.e. the flow is almost perpendicular to the axis of the riser in its equilibrium configuration.

With the model described in Section 2, simulations are performed for the VIV of a riser under initial top tension $T = 810$ N at different flow velocities ranging from 0.1 m/s to 1.0 m/s, with a step of 0.02 m/s, resulting in a total of 45 cases. The values of the hydrodynamic force coefficients C_{L0}, C_{D0} and $\overline{C}_D$ are not reported in [30] and [37]. Therefore, the same values as used in [1], namely $C_{L0} = 0.3$, $C_{D0} = 0.1$, $\overline{C}_D = 1.2$, are applied here. As to the Strouhal number St, a value St $= 0.17$ is taken as given in [30]. The riser is discretised into 50 elements, and a convergence test has been conducted to assure the accuracy of the discretisation. For each case, the flow velocity is applied in a ramped manner, and the simulation time is chosen such that a minimum time window of steady-state response corresponding to at least 50 vortex shedding cycles (following the Strouhal relation) is achieved.

3.2 Comparison of predictions and experimental measurements

Non-dimensional parameters have been used to present the simulation results. To illustrate the variation of riser response with respect to the flow velocity, two different types of reduced velocity have been applied. The first type, V_1, is calculated using the fundamental natural frequency f_1 in still water, while the second type is obtained based on the dominant response frequency for the cross-flow f_y and in-line f_x:

$$V_1 = \frac{V}{f_1 D} \tag{56}$$

$$V_{x,y} = \frac{V}{f_{x,y} D}. \tag{57}$$

The fundamental frequency f_1 is calculated using the finite element model under the riser's initial vertical configuration in still water, subjected to a mean top tension obtained over the time window that has been chosen for analysis. The dominant response frequency is defined as the frequency of the dominant mode. The same modal analysis approach as used in [38] has been adopted here to determine the dominant modes. The modal shapes of the riser used in the modal analysis are calculated under an initial vertical position in still water, with the averaged top tension obtained over the time window that has been chosen for analysis. The use of the term 'modes' here is not rigorous, as the riser will vibrate around its in-line offset due to the drag force, and the top tension is also not constant during the vibration. More importantly, the added mass is not the same in the current as that in the still water. Therefore,

the 'modes' used here are only a reasonable approximation. As for the indications of response amplitudes, the cross-flow response standard deviation σ_y and σ_x for in-line, has been calculated as follows [37]:

$$\sigma_{x,y} = \sqrt{\frac{1}{S}\sum_{j=1}^{S}\left[\frac{1}{N}\sum_{i=1}^{N} u_{ji}^2\right]} \tag{58}$$

where S is the number of time samples, N is the number of locations along the riser where the response of the riser is read, u_{ji} denotes the displacement of riser at location i and time instance j and only the fluctuating component of the in-line displacement is considered.

With Eq.(58), the standard deviations of cross-flow and in-line response amplitudes (with the mean in-line deflection subtracted) have been calculated, and they are shown in Fig.5 against reduced velocity V_1. In simulation results, both single and multiple frequency responses are observed. The cases of single frequency response are represented by hollow diamonds, while those of multiple frequency response are represented by black squares. For the multiple frequency response, the standard deviations of the in-line displacement are obtained after removing the low frequency components through a high pass filter. The standard deviations of the simulated cross-flow and in-line displacements are plotted in Fig.5. Following the same approach taken by Chaplin et al. [30], the results are grouped according to the combination of dominant in-line and cross-flow modes represented by the arrows with dashed lines, and the thick grey lines represent the linear approximation of the experiment results.

As can be seen from Fig.5, the standard deviations of the simulated amplitudes appear to be slightly scattered, with most cross-flow values varying from $0.1D$ to $0.4D$, which is in good agreement with the experimental measurements. The standard deviations of the simulated in-line amplitudes, which mostly lie between $0.04D$ and $0.12D$, are generally smaller than those from the experiments. The underestimation of the in-line amplitude by the same wake oscillator model was also reported in the prediction of free vibration of the rigid cylinder [1]. This is one drawback of the model which needs further improvement.

In general, the response of the riser predicted by the model follows the same pattern as those observed in the experiments. For both cross-flow and in-line displacements, there is a trend of increase with an increased reduced velocity within each group. As the reduced velocity further increases beyond the group, the subsequent group takes over and starts at a much smaller amplitude, generating discontinuities and jumps between groups. Overlaps of groups are also observed, and

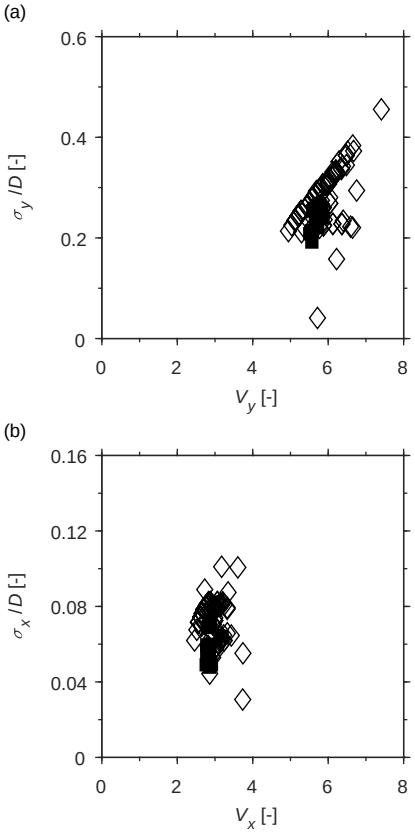

Fig. 6: Standard deviations of (a) cross-flow and (b) in-line displacements against reduced velocity $V_{x,y}$.

multiple frequency response usually takes place within these regions. For the cross-flow response, although some discrepancies are observed between the simulated results and experimental measurements, the agreement is consider to be qualitatively good for reduced velocities $V_1 > 20$. However, at small reduced velocities where the cross-flow mode up to the third is dominant, the simulated cross-flow amplitudes are significantly smaller than those in the experimental measurements, and the increasing trends, represented by the slopes of the lines, are much less sharp. This may be due to the fact that in the experiments, all the measurements at small reduced velocities, corresponding to mode patterns 2/1, 4/2 and 6/3, are obtained at top tensions that are much higher than the one used in the simulations.

In Fig.6, the standard deviations of simulated cross-flow and in-line displacement are now plotted against the reduced velocities based on the dominant frequency $f_{x,y}$. The cross-flow response falls in the region between $V_y = 5$ and $V_y = 7$, while the in-line response collapses around $V_x = 3$. A clear trend of increasing amplitude with reduced velocity is observed in the cross-flow direction, while it is much less significant in the in-line direction.

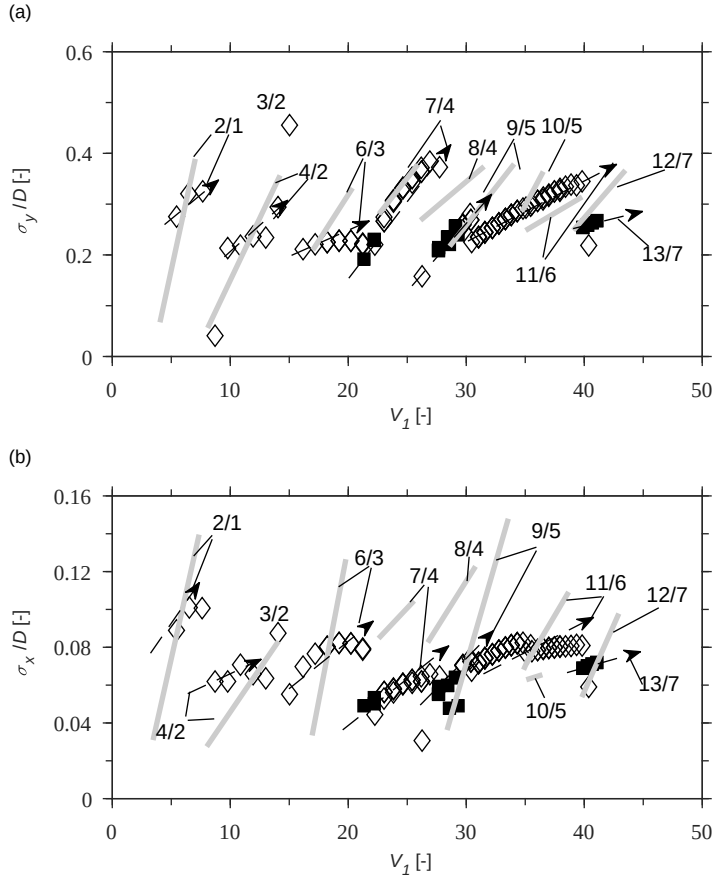

Fig. 5: Standard deviations of (a) cross-flow and (b) in-line displacements. Simulation results are represented by hollow diamonds (single frequency response) and black squares (multiple frequency response). Simulation results are grouped by the arrows with dashed lines labeled with (dominant in-line modes)/(dominant cross-flow modes). Linear approximation of the experimental results in [30] are represented by grey thick lines.

The dimensionless frequency, which is obtained by normalising the dominant frequency in the form $f_{x,y}D/V$, is plotted in Fig.7 against the reduced velocity V_1. In general, the cross-flow response is around the Strouhal frequency, which is represented by the straight line in Fig.7(a) at 0.17. The in-line dominant frequency, on the other hand, is always double that of the cross-flow frequency, and it concentrates around 0.34. Thick grey lines in the figure represent reasonable linear approximations of the experimental results, indicating the range as well as the variation of the measured dominant frequencies, which are in good agreement with the simulation results. The main difference between the two is observed at high reduced velocities where the experimental results display a trend of becoming more concentrated around the Strouhal frequency, while those of the simulations still spread over a wide range of reduced velocities.

The jumps of the dimensionless frequency is due to the lock-in, which is illustrated in a better way in Fig.8 where the frequency is normalised by the fundamental frequency. A clear stair-stepping trend in the dimensionless frequency of both cross-flow and in-line responses is noticeable.

In Fig.9, the simulated dominant modes as well as those observed in the experiments are plotted. The comparison of the simulation and experiment results reveals good agreements between the two regarding the cross-flow dominant modes. As for the in-line dominant modes, at low reduced velocities, both simulation and experiment results demonstrate that only even-numbered modes appear. For high reduced velocities, both even and odd-numbered modes are observed from the experiments while, interestingly, only odd modes appear in the simulations.

The reason for only the odd-numbered modes to be predicted by the model at high reduced velocities is still unclear to the authors and requires further study.

With regard to the in-line offset of the riser, since the drag force is proportional to the square of the flow speed, it is expected that the maximum in-line deflection should follow a similar trend. In Fig.10, the mean of the maximum in-line deflections $\tilde{x}_{max}$ are plotted against the reduced velocity V_1, and a general quadratic relationship between the two can be found. $\tilde{x}_{max}$ is obtained by finding the maximum in-line deflections along the riser at each time instance and then taking the mean value of these maxima. The line shows that the best quadratic fit to the results yields a coefficient

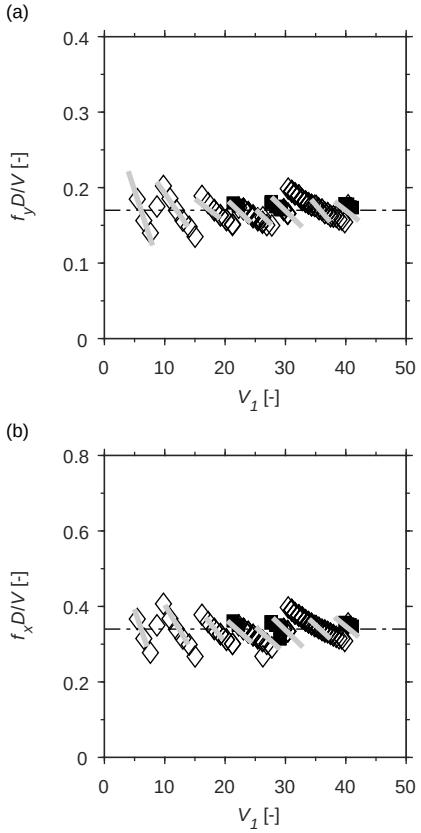

Fig. 7: Normalised (a) cross-flow and (b) in-line dominant frequencies ($f_{x,y}D/V$) versus V_1. In (a), the straight line represents the frequency corresponding to a Struhal number 0.17; and in (b), the straight line represents the doubled frequency corresponding to a Struhal number 0.17. Linear approximation of the experimental results by [37] are represented by grey thick lines.

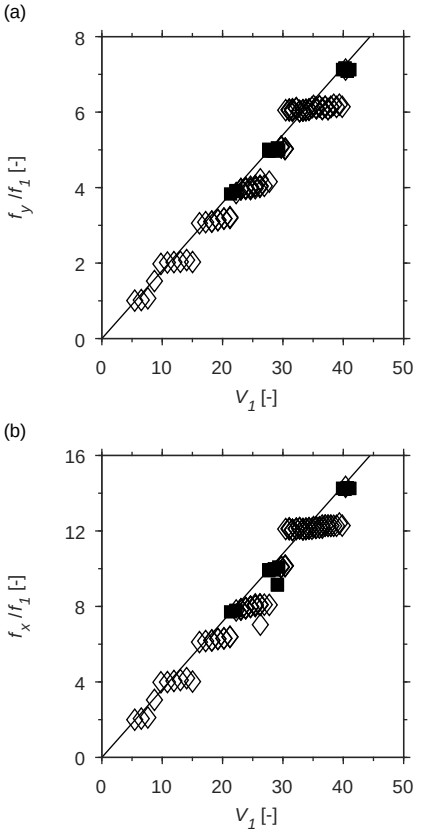

Fig. 8: Normalised (a) cross-flow and (b) in-line dominant frequencies ($f_{x,y}/f_1$) versus V_1. In (a), the straight line represents the frequency corresponding to a Struhal number 0.17; and in (b), the straight line represents the doubled frequency corresponding to a Struhal number 0.17.

of 6.7e^{-3}, which is in excellent agreement with the experimental measurements where a coefficient of 6.1e^{-3} was obtained [37]. This proves that the amplification of the in-line force due to VIV is properly captured by the model. This reveals one of the main advantages of the current model over the original one without in-line coupling [18], which has been shown in [39] and [40] to significantly underestimate the mean in-line deflection of the riser.

3.3 Predicted single and multiple frequency responses

For a flexible riser that is subjected to the uniform flow, despite the fact that several modes may potentially be excited, it is normally expected that one will eventually dominate, and the motion of the riser would be characterised as a single frequency response. Although in the case of experiments to be simulated in this section, only half of the riser is subjected to flow, the behaviour of the riser should follow the same pattern, since it is expected that only one vortex shedding frequency is involved. However, the simulation results of the experiments reveal the presence of both single and multiple frequency responses. The multiple frequency response is normally observed within the range of flow velocities where the riser response is in transition from one mode to another,as can be seen in Fig.5. In what follows, two examples of riser responses at two different flow velocities $V = 0.5$ m/s and $V = 0.56$ m/s are presented to illustrate the typical single and multiple frequency responses observed in the simulation results.

Case 1: $V = 0.5$ m/s, single frequency response.

An example of a simulated single frequency response is demonstrated here at flow velocity $V = 0.5$ m/s. The spatial and temporal characteristics of the structural response are analysed based on a 2D Fourier transform. Denoting the cross-flow displacement of the riser as $y\,(p/L, t)$, where p is the coordinate along the riser and L is the length of the riser, the 2D Fourier Transform

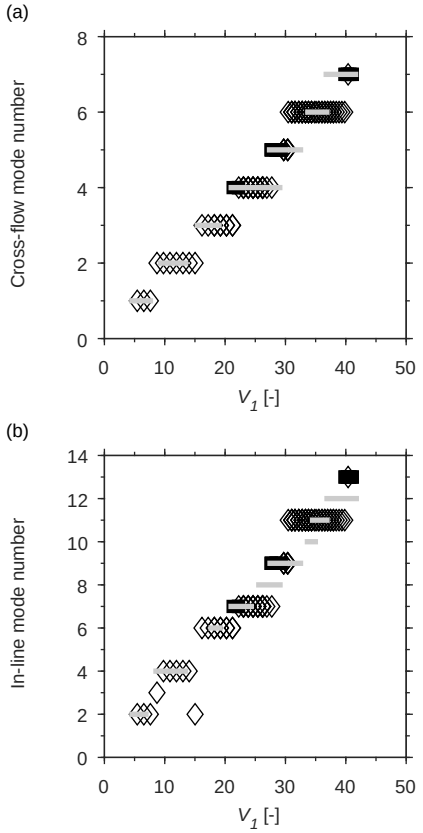

Fig. 9: Dominant mode for (a) cross-flow and (b) in-line displacements. Linear approximation of the experimental results by [37] are represented by grey thick lines.

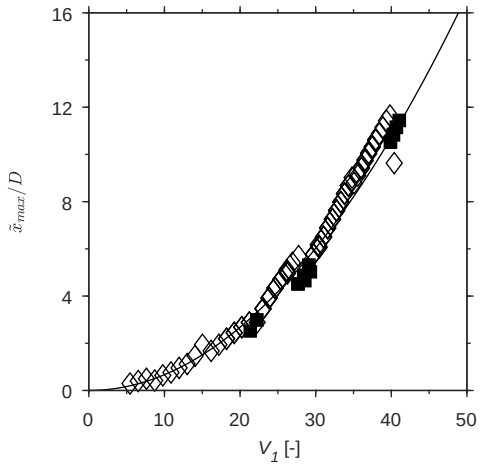

Fig. 10: Mean of maximum in-line deflection. The curve shows the best quadratic fit to the results with the expression $\tilde{x}_{max}/D = 6.7\mathrm{e}^{-3}V_1^2$

of the displacement is defined as

$$\tilde{\mathbf{y}}\left(f,k\right) = \frac{1}{L}\int_0^L \int_0^{T_0} y\left(p/L,t\right)\mathrm{e}^{-\mathrm{i}2\pi ft}\mathrm{e}^{-\mathrm{i}2\pi kp/L}dtdp \tag{59}$$

where f is the frequency, k is the dimensionless wavenumber and T_0 is the duration of the data set. The above equation is the Continuous Fourier Transform and for the discrete displacements, as those obtained from the simulation, the Discrete Fourier Transform (DFT) has been applied. The 2D DFT of the in-line displacement, with the mean in-line deflection subtracted, is calculated in the same way. In the following part, the 2D spectrum of the displacement of the riser is presented in the form of power spectral density (PSD), which is obtained as $|\tilde{\mathbf{y}}|^2/T_0$.

In Figs.11(a) and (b), the 2D PSD of cross-flow and in-line non-dimensional displacements are presented against the frequency and spatial wavenumber. The PSD is normalised by its maximum value. The frequency of oscillations – f_y for the cross-flow and f_x for the in-line – is normalised by the Strouhal frequency $f_s = \mathrm{St}V/D$. Only the positive frequency is presented in Figs.11(a) and (b), and positive wavenumbers are thus associated with travelling waves propagating towards $p/L = 0$ (downwards), while negative wavenumbers are associated with travelling waves moving in the opposite direction. Figs.11(a) and (b) also illustrate the wavenumbers of free vibration structural modes, indicated by vertical dashed lines, and the corresponding natural frequencies, indicated by red crosses, which are calculated using the finite element model described in the previous section. The modal shape and natural frequencies of the structure are obtained under the initial straight configuration under top tension that is equal to the mean value of the simulated varying top tension. Due to the variation of the tension along the riser as a result of gravity, the structural mode shapes are slightly different from sinusoidal shapes. For the sake of simplicity, the wavenumbers of the structural modes are still approximated using sinusoidal mode shapes.

As can be seen from Figs.11(a) and (b), the structural response is dominated by a single frequency in both the cross-flow and in-line directions. In the cross-flow direction, the riser oscillates at a peak frequency $f_y = 0.877f_s$, and the in-line motion is dominated by the frequency $f_x = 1.754f_s$, which is twice that of the cross-flow motion. The excited wavenumbers, different from the frequency that concentrates around a single value, seem to spread over a relatively wide range. This is partially caused by the numerical errors of DFT conducted in the space domain, as only a small number of

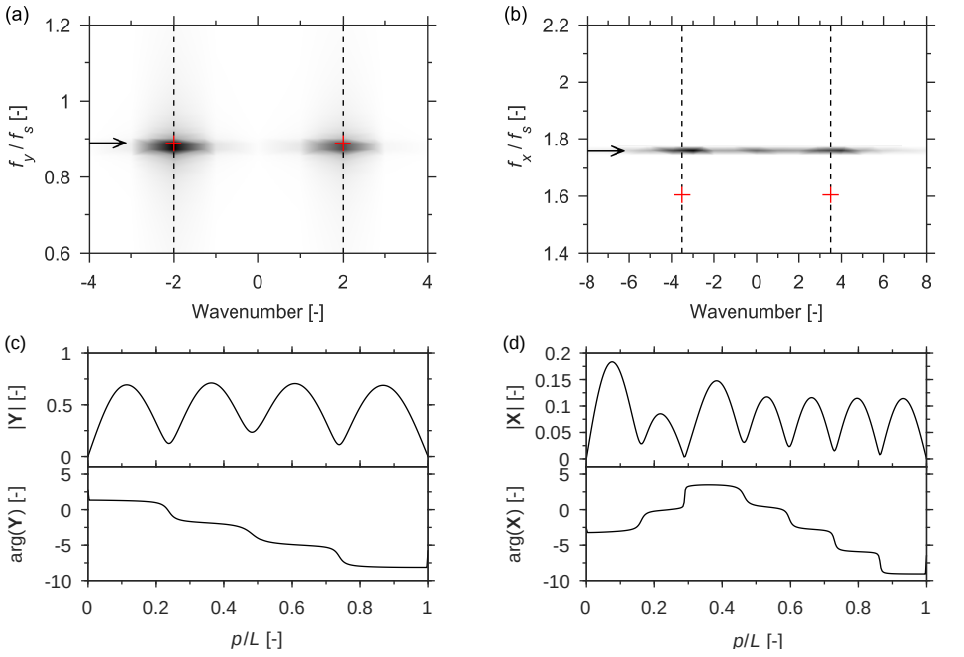

Fig. 11: Spatio-temporal spectra of (a) cross-flow and (b) in-line displacements at flow velocity $V = 0.5$ m/s with (c) cross-flow and (d) in-line complex modes extracted at dominant frequencies which are indicated by arrows. The wavenumbers and natural frequencies of selected free vibration modes are indicated by black vertical dashed lines and red crosses respectively.

spatial cycles are excited along the riser, and partially because of the variation of the top tension in time. Therefore, it is difficult to determine from Figs.11(a) and (b) the exact wavenumber at which the structure vibrates. In such cases, the complex modes extracted at the dominant frequency, as will be demonstrated later, are taken as references to decide on the main dominant wavenumber.

It is clear from Fig.11(a) that in the cross-flow direction, the riser vibrates at a wavenumber and a frequency that are both close to the 4th free vibration mode, while in the in-line direction, as illustrated in Fig.11(b), the wavenumber close to the 7th free vibration mode is excited, but at a lower frequency than the corresponding natural frequency. It is conventionally expected that a single structural wavenumber will be excited at a given frequency, which is the case for the cross-flow motion. However, in the in-line direction, apart from the wavenumber close to 3.5, another wavenumber close to zero is also excited at the same frequency. This is because the top of the riser is not constrained in the vertical direction, and its vibration, at the same frequency of the in-line motion, leads to the periodic variation of the in-line offset, which resembles the shape corresponding to small wavenumbers.

The slightly different weights of positive and negative wavenumber peaks suggest that the response of the structure is characterised by mixed standing-travelling waves. To further investigate the pattern of the riser response, the response modes of the structure are calculated using Fourier expansion following the same approach as given in [41]. Denoting the cross-flow displacement of the riser as $y(p_r, t_j)$, the Fourier expansion of the times series of $y(p_r, t_j)$ at location p_r is given as:

$$y(p_r, t_j) = \mathrm{Re}\left(\sum_{l=1}^{\Lambda} \hat{y}(p_r, \omega_l)\, \mathrm{e}^{\mathrm{i}\omega_l t_j}\right) \tag{60}$$

where $\hat{y}(p_r, \omega_l)$ is complex-valued and represents the l^{th} Fourier coefficient corresponding to the frequency ω_l. Extracting $\hat{y}(p_r, \omega_l)$ at each location along the riser, one obtains the cross-flow response mode of the riser at a specific frequency ω_l, denoted as $\mathbf{Y}(p_r)$. The same process can be applied to the in-line motion to obtain the in-line response mode of the riser denoted as $\mathbf{X}(p_r)$.

The spanwise evolution of amplitudes and phase angles of the response modes $\mathbf{Y}(p_r)$ and $\mathbf{X}(p_r)$, is presented in Figs.11(c) and (d), for the dominant frequencies shown in Figs.11(a) and (b). The shapes of $|\mathbf{Y}(p_r)|$ and $|\mathbf{X}(p_r)|$ suggest that both cross-flow and in-line motions are dominated by the standing wave. However, the absence of the definite nodes reveals the underlying travelling character of the riser response in both directions. The cross-flow vibration, as depicted in Fig.11(c), is close to the 4th free vibration mode, while the in-line vibration exhibits a different pattern compared to the 7th mode, as can be seen in Fig.11(d). The underlying travelling character of the structural response can be better illustrated by the evolution of the phase of the complex modes. For the cross-flow motion, the general decreasing trend of the phase angle corresponds to travelling waves moving from $p/L = 0$ towards $p/L = 1$ (upwards). This is consistent with the fact that only

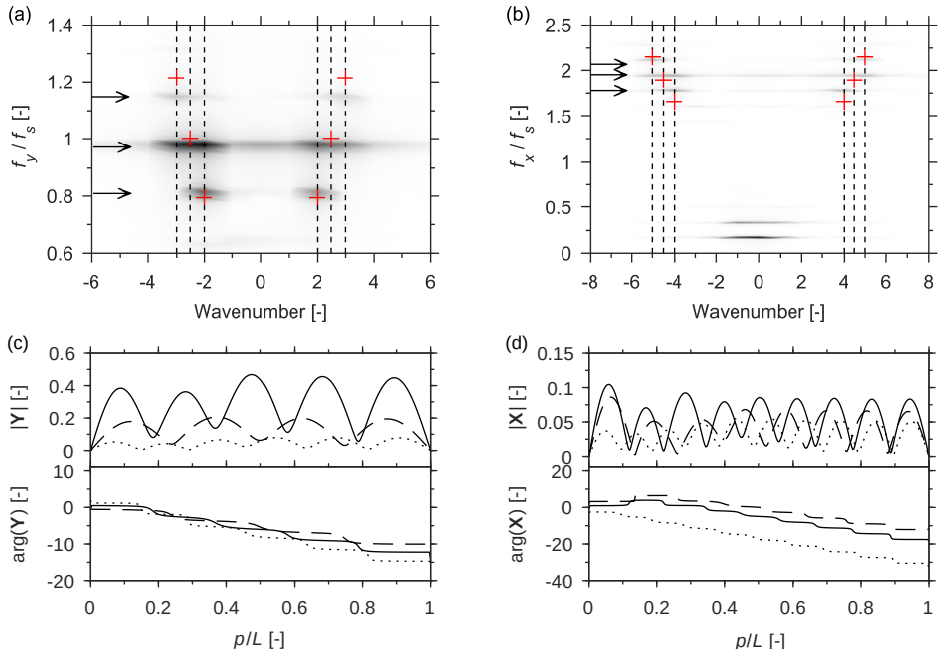

Fig. 12: Spatio-temporal spectra of (a) cross-flow and (b) in-line displacements at flow velocity $V = 0.56$ m/s with (c) cross-flow and (d) in-line complex modes extracted at dominant frequencies which are indicated by arrows. The wavenumbers and natural frequencies of selected free vibration modes are indicated by black vertical dashed lines and red crosses respectively. In (c) dash line – $f_y = 0.810f_s$; solid line – $f_y = 0.975f_s$; dot line – $f_y = 1.145f_s$. In (d) dashed line – $f_y = 1.780f_s$; solid line – $f_y = 1.949f_s$; dotted line – $f_y = 2.117f_s$.

the bottom half of the riser is subjected to the flow, and the energy should therefore be input over the same segment, carried away in the form of a travelling wave and dissipated over the upper half of the riser which is submerged in the still water and only subjected to damping. The spanwise evolution of the phase angle of the in-line response mode indicates that the wave is excited close to $p/L = 0.4$ – still within the bottom half of the riser–and propagates in two directions towards both boundaries.

Case 2: $V = 0.56$ m/s, multiple frequency response.

Although a single frequency response is observed for most simulation cases, for a few, especially those within the range of flow velocities where the riser response is in transition from one mode to another, a multi-frequency response is detected. An example of a simulated multi-frequency response is given here at flow velocity $V = 0.56$ m/s, which lies in the transition of the cross-flow dominant mode from the 4th to the 5th mode. The 2D PSD of the steady-state riser response and the response modes of the dominant frequency are presented in Fig.12.

As can be seen from Figs.12(a) and (b), the riser exhibits a response at several frequencies in both the cross-flow and in-line directions. The cross-flow response, as illustrated in Fig.12(a), has main peaks at frequencies $f_y = 0.810f_s$, $0.975f_s$ and $1.145f_s$. Most energy concentrates at the frequency $f_y = 0.975f_s$, which is the closest of the three frequencies to the Strouhal frequency. The secondary dominant frequency is $f_y = 0.810f_s$. At frequency $1.145f_s$, only small peaks are observed. The frequencies $f_y = 0.810f_s$ and $0.975f_s$ are close to the 4th and 5th natural frequencies of the structure respectively, and the wavenumbers excited at these two frequencies are consistent with the corresponding free vibration modes. At frequency $f_y = 1.145f_s$, the response of the riser deviates from the 6th natural frequency, although the excited wavenumber is close to the 6th free vibration mode.

Concerning the in-line response, as portrayed in Fig. 12(b), apart from the frequency components around $2f_s$ as expected, significant energy concentrates at low frequencies of $f_x = 0.25f_s$ and $0.3f_s$. The source of these low frequency components will be discussed later. Three main frequency peaks are observed around $2f_s$: $f_x = 1.780f_s$, $1.949f_s$ and $2.117f_s$. Comparing these in-line frequencies with their cross-flow counterparts leads to ratios of $f_x/f_y = 2.20$, 2.00 and 1.85 respectively. Only the cross-flow frequency close to the Strouhal frequency apparently has a ratio of $f_x/f_y = 2$. All three in-line frequency-wavenumber pairs would not result from the free vibration analysis.

In Figs.12(c) and (d), the response modes of cross-flow and in-line response at frequencies – which are indicated by arrows in Figs.12(a) and (b) – are presented. Again, the well-defined cells in the amplitudes of the response modes – both cross-flow and in-line – suggest that the response of the riser at each frequency is dominated by standing waves. The response modes with the highest magnitude are at frequencies that are close to the Strouhal frequency (double the Strouhal frequency for the in-line response). The underlying travelling

character of the response can be observed in the variations of the phase angle along the riser, which suggests that the waves are excited within the bottom half of the riser and move towards the upper end, and the travelling waves seem to be more pronounced in the in-line response.

One interesting question that arises is whether the multi-frequency response is a result of coexisting multiple frequency components or a result of only one frequency that varies in time. To answer this question, the wavelet transform is performed for selected time series of cross-flow and in-line displacements at locations $p/L = 0.9$ and 0.95 respectively, where all dominant frequencies make significant contributions; the results are plotted in Fig.13. In these plots, the predominant response frequencies identified in the previous analysis are indicated by dashed lines, and for in-line vibration, only the frequency components around $f_x/f_s = 2$ are displayed. It is clear from Fig.13 that in the cross-flow response, the multiple frequency components instantaneously coexist and remain independent over the entire observation period, while those of the in-line vibration are characterised by a main dominant frequency that sweeps up and down across the dashed lines over time.

The multiple frequency response predicted by the proposed model for the VIV of a flexible cylinder fully or partially subjected to a uniform flow has been scarcely reported in the literature. The main reason, according to the authors, is the difficulty in capturing and quantifying it in the experiments. First, the multiple frequency response is normally observed in the transition region, which requires a small increment of flow velocity to be captured. Second, the multiple frequency response seems to be fragile, and the balance between the different coexisting frequency components can be easily jeopardised by, for example, external disturbance. Finally, even though the multiple frequency response is observed in experiments, it is difficult to decide whether it corresponds to a steady response or a transition phase. Therefore, in most experiments, for example the one by Chaplin et al. [30], only the time segment corresponding to a steady periodic motion with a constant amplitude is chosen for post processing; however, strong modulation of the response of the structure is observed in other time segments.

To the authors' best knowledge, this multiple frequency VIV in uniform flow is only reported in the work by Seyed-Aghazadeh et al. [42]. In their experiments, a uniform flexible cylinder is placed vertically in a re-circulating water tunnel subjected to a uniform flow. Only low modes of the structure are excited, and the flow velocity is increased in small increments. Seyed-Aghazadeh et al. [42] report that at a small reduced velocity, only first-mode excitation is observed in the cross-flow response of the cylinder. As the reduced velocity increases to a certain value, a second harmonic contribution, in addition to the first one, with the second structure mode shape is observed. The contribution from the second harmonic monotonically increases with increasing flow velocity and finally becomes dominant over the first mode.

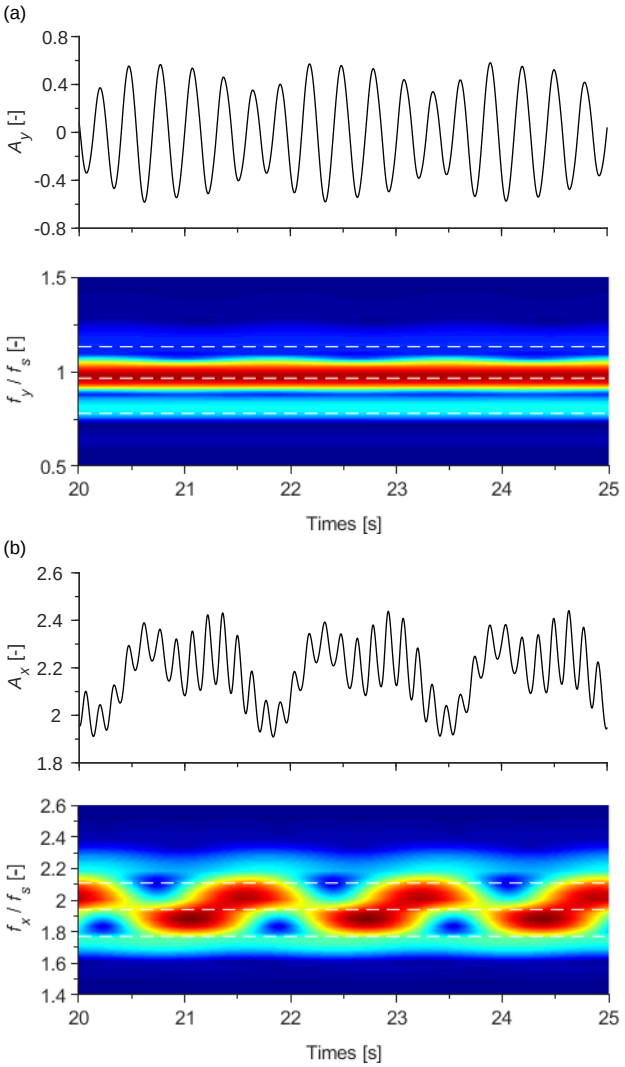

Fig. 13: Selected time series of (a) cross-flow and (b) in-line displacements, and corresponding frequency content as a function of time. The dashed lines represent the dominant frequencies indicated by arrows in Fig. 12.

It is a pity that in the work [42], although the frequency content of the in-line motion demonstrates a significant contribution from low frequencies when the transition occurs – see Fig.4(f) in [42] – it is not clear whether this is due to the multiple frequency response or if it is simply the result of a mean in-line deflection due to the drag force. Gopalkrishnan [10] has already

demonstrated that for a rigid cylinder that is forced to vibrate with a prescribed beating motion, the 'instantaneous mean drag force coefficient', defined as the average value of the drag coefficient over one carrier frequency, follows the envelope of the beating motions. If the fluid-structure interaction for a flexible cylinder is similar to that of a rigid cylinder, then it is reasonable to expect that the modulation of the cross-flow motion would lead to the slow variation of the in-line force that follows its envelope and consequently results in a low frequency component in the in-line motion.

4 Conclusions

In this paper, a nonlinear model has been presented for the simulation of coupled cross-flow and in-line VIVs of flexible cylindrical structures. The structure is described as a geometrically nonlinear extensible Euler-Bernoulli beam, and the interaction between the structural motion and fluid is modelled by a wake oscillator, with nonlinear in-line and linear cross-flow coupling, that is uniformly distributed along the cylinder. Although the main focus has been on the VIV of a straight flexible cylinder, the same model can, in principle, be used for the prediction of the VIV of a curved structure, such as a catenary riser. To deal with the cases where the incident flow is not perpendicular to the cylinder axis, a local coordinate frame is introduced, and the independence principle is applied.

The dynamics of the coupled system has been analysed using the finite element method, and the simulation results of a series of experiments where a top-tensioned flexible riser was subjected to step flows have been presented. A comparison with the experimental results has revealed that the model is able to qualitatively predict most features of VIVs of flexible cylinders, and the predicted vibration amplitudes, frequencies and excited modes are in good agreement with the measurements. Moreover, it has been demonstrated that the current model is able to offer good prediction of the mean in-line deflections, which reflects its superiority over the original model proposed in [18] without in-line coupling, as the latter one significantly underestimates the amplification of the mean in-line force when VIV occurs.

In contrast to the conventional belief that the VIV of a flexible cylinder subjected to a uniform flow should be dominated by a single frequency oscillation, the current model predicts that over the range of flow velocities through which a transition of the dominant mode of vibration takes place, the riser may exhibit a multi-frequency response. In such cases, the multiple frequency components in the cross-flow response instantaneously coexist, while those of the in-line response are the result of a single frequency that temporally drifts from one predominant frequency to another one. When the multi-frequency response occurs, the in-line response contains significant components at a low frequency, which is caused by the slow variation of the in-line force due to the modulation of the cross-flow displacements.

Acknowledgements The first author would like to thank the China Scholarship Council (CSC) (No. 201206450001) and the National Natural Science Fundation of China (Grant No. U19B2013) for the financial support to this work.

Conflict of interest

The authors declare that they have no conflict of interest.

Appendix A A preliminary study on the effect of frequency ratio on the coupled cross-flow and in-line VIV of an elastically supported rigid cylinder

In this appendix, a preliminary study is conducted to compare the performance of two different sets of tuning parameters, which have been used in previous study [1], in the modelling of coupled cross-flow and in-line VIV of an elastically supported cylinder with unequal natural frequencies in cross-flow and in-line directions. In this preliminary study, simulations of VIVs of a rigid cylinder are conducted with the ratio between the in-line and cross-flow natural frequencies increasing from 1 to 2.5. The set of parameters that reproduces the main features of the VIV observed in the experiments would be adopted in the paper for the modelling of VIVs of flexible cylinders.

Fig.14 displays the two-dimensional VIV of an elastically supported rigid cylinder placed in a steady and uniform flow. The displacements of the cylinder X and Y along the in-line and cross-flow directions can be described as

$$(m+m_a)\frac{\mathrm{d}^2X}{\mathrm{d}t^2}+b_x\frac{\mathrm{d}X}{\mathrm{d}t}+k_xX=LF_{VX} \tag{61}$$

$$(m+m_a)\frac{\mathrm{d}^2Y}{\mathrm{d}t^2}+b_y\frac{\mathrm{d}Y}{\mathrm{d}t}+k_yY=LF_{VY} \tag{62}$$

where m is the mass of the cylinder, L is the length of the cylinder and $m_a=\rho\pi LD^2C_a/4$ ($C_a=1$) is the added mass.

Dividing equations by $(m+m_a)$ and introducing cross-flow and in-line force coefficients C_{VY} and C_{VX},

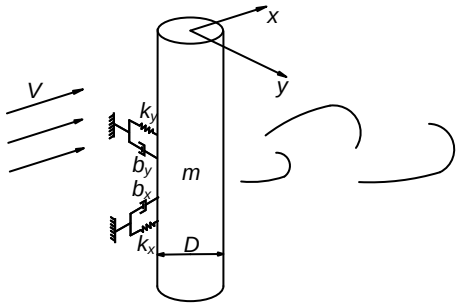

Fig. 14: A schematic diagram of coupled cross-flow and in-line VIV of an elastically mounted circular cylinder in uniform flows.

Eqs. (61) and (62) become

$$\frac{d^2X}{dt^2} + 2\zeta_x\omega_{xn}\frac{dX}{dt} + \omega_{xn}^2 X = \frac{1}{2}\rho DLV^2\frac{C_{VX}}{m+m_a} \quad (63)$$

$$\frac{d^2Y}{dt^2} + 2\zeta_y\omega_{yn}\frac{dY}{dt} + \omega_{yn}^2 Y = \frac{1}{2}\rho DLV^2\frac{C_{VY}}{m+m_a} \quad (64)$$

where $\omega_{(x,y)n} = \sqrt{k_{x,y}/\left(m+m_a\right)}$ and $\zeta_{x,y} = b_{x,y}/\left(2\omega_{(x,y)n}\left(m+m_a\right)\right)$ are the natural frequency and damping ratio of the cylinder in still water and C_{VY} and C_{VX} are given by Eqs.(17) and (18) respectively.

Eqs.(63), (64), (17), (18) and (23) formulate the initial value problem for the coupled cross-flow and in-line VIV of an elastically supported rigid cylinder.Using the following quantities:

$$\tau = \omega_s t, \Omega_{(x,y)n} = \omega_{(x,y)n}/\omega_s, x = X/D, y = Y/D \quad (65)$$

the dimensionless form of the governing equations is obtained as

$$\ddot{x} + 2\zeta_x\Omega_{xn}\dot{x} + \Omega_{xn}^2 x = \frac{C_{VX}}{2\pi^3\mathrm{St}^2\left(m^*+C_a\right)} \quad (66)$$

$$\ddot{y} + 2\zeta\Omega_{yn}\dot{y} + \Omega_{yn}^2 y = \frac{C_{VY}}{2\pi^3\mathrm{St}^2\left(m^*+C_a\right)} \quad (67)$$

$$\ddot{q} + \epsilon(q^2-1)\dot{q} + q - \kappa\frac{\ddot{x}}{1+\ddot{x}^2}q = A\ddot{y} \quad (68)$$

where

$$\begin{aligned} C_{VX} =& \left(C_{VD}\left(1-2\pi\mathrm{St}\dot{x}\right) + C_{VL}2\pi\mathrm{St}\dot{y}\right) \\ & \sqrt{\left(1-2\pi\mathrm{St}\dot{x}\right)^2 + \left(2\pi\mathrm{St}\dot{y}\right)^2} \\ & + \alpha C_{VL}^2\left(1-2\pi\mathrm{St}\dot{x}\right)\left|1-2\pi\mathrm{St}\dot{x}\right| \end{aligned} \quad (69)$$

$$\begin{aligned} C_{VY} =& \left(-C_{VD}2\pi\mathrm{St}\dot{y} + C_{VL}\left(1-2\pi\mathrm{St}\dot{x}\right)\right) \\ & \sqrt{\left(1-2\pi\mathrm{St}\dot{x}\right)^2 + \left(2\pi\mathrm{St}\dot{y}\right)^2} \end{aligned} \quad (70)$$

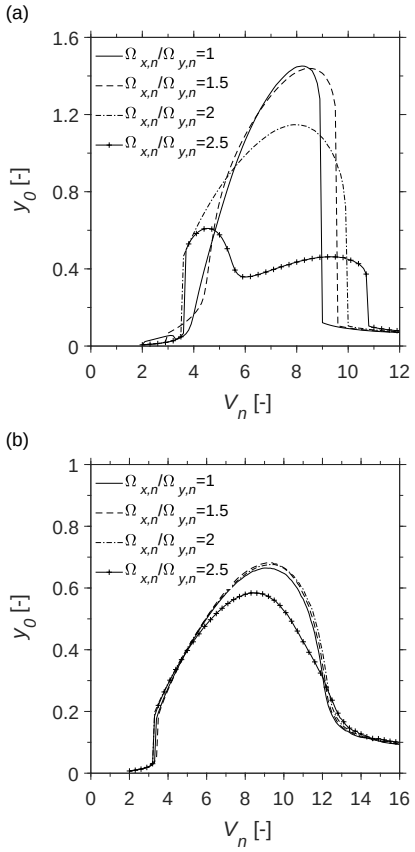

Fig. 15: Influence of the frequency ratio $\Omega_{x,n}/\Omega_{y,n}$ on the cross-flow response using tuning parameters of (a) Case U ($A=8$, $\epsilon=0.08$, $\kappa=5$) and (b) Case L ($A=20$, $\epsilon=0.8$, $\kappa=5$)

and $m^* = m/\left(\rho\pi D^2/4\right)$ is the mass ratio and the overdots denote derivatives with respect to the dimensionless time τ.

With the definition of C_{VD} and C_{VL} given by Eq.(21) and (24), Eq.(66-70) can be solved numerically in the time domain, using a fifth-order Runge-Kutta method, to simulate the coupled cross-flow and in-line VIV of an elastically supported rigid cylinder.

Using the same empirical parameters given in [1], simulations have been conduced with $m^* = 2.6$ and $\xi_{x,y} = 0.005$ for $\Omega_{nx}/\Omega_{ny} = 1-2.5$. Two different sets of tuning parameters Case U and Case L have been applied and the amplitude of the dimensionless cross-flow displacement y_0 are plotted in Fig.15 against reduced velocity $V_n = 2\pi V/\left(\omega_{yn}D\right)$.

For the results of Case U, as can be seen in Fig.15(a), the maximum amplitude of the cross-flow vibration significantly decreases as the frequency ratio increases from 1 to 2.5. Meanwhile, the range of lock-in is extended. Especially, the amplitude of the cross-flow vibration is characterized by two peaks at frequency ratio 2.5. For the results of Case L, as can be seen in Fig.15(b), the

frequency ratio only has a small influence on the cross-flow response which decreases slightly as the frequency ratio increases. The results of Case U is qualitatively more consistent with the experimental observations as reported in [35]. Therefore, the corresponding tuning parameters are adopted in this paper to model the coupled cross-flow and in-line VIVs of flexible cylinders.

Appendix B Finite element formulation and time integration

B.1 Derivation of the stiffness matrix of the beam element

Substituting the variation of ϵ_0 and K, given by Eq. (7), and (8) into Eq. (4) yields

$$\begin{aligned}\delta W_S = \int_0^L \Big[& EA\frac{|\mathbf{r}_{,p}|-1}{|\mathbf{r}_{,p}|}\mathbf{r}_{,p}^{\intercal}\delta\mathbf{r}_{,p} \\ & -2EI\frac{|\mathbf{r}_{,p}\times\mathbf{r}_{,pp}|^2}{|\mathbf{r}_{,p}|^6}\mathbf{r}_{,p}^{\intercal}\delta\mathbf{r}_{,p} \\ & +EI\frac{(\mathbf{r}_{,p}\times\mathbf{r}_{,pp})^{\intercal}}{|\mathbf{r}_{,p}|^4}\left(\delta\mathbf{r}_{,p}\times\mathbf{r}_{,pp}+\mathbf{r}_{,p}\times\delta\mathbf{r}_{,pp}\right)\Big]\,dp\end{aligned} \tag{71}$$

In three dimensions, Binet-Cauchy identity asserts that, for four vectors $\mathbf{a}$, $\mathbf{b}$, $\mathbf{c}$ and $\mathbf{d}$, the following relation holds

$$(\mathbf{a}\times\mathbf{b})^{\intercal}(\mathbf{c}\times\mathbf{d}) = (\mathbf{a}^{\intercal}\mathbf{c})(\mathbf{b}^{\intercal}\mathbf{d}) - (\mathbf{a}^{\intercal}\mathbf{d})(\mathbf{b}^{\intercal}\mathbf{c}) \tag{72}$$

Applying Binet-Cauchy identity to Eq. (71), one obtains

$$\begin{aligned}\delta W_S = \int_0^L \Big[& EA\left(1-\frac{1}{|\mathbf{r}_{,p}|}\right)\mathbf{r}_{,p}^{\intercal}\delta\mathbf{r}_{,p} + EI\frac{1}{|\mathbf{r}_{,p}|^2}\mathbf{r}_{,pp}^{\intercal}\delta\mathbf{r}_{,pp} \\ & -EI\frac{1}{|\mathbf{r}_{,p}|^4}|\mathbf{r}_{,pp}|^2\mathbf{r}_{,p}^{\intercal}\delta\mathbf{r}_{,p} \\ & -EI\frac{1}{|\mathbf{r}_{,p}|^4}\mathbf{r}_{,p}^{\intercal}\mathbf{r}_{,pp}\left(\mathbf{r}_{,pp}^{\intercal}\delta\mathbf{r}_{,p}+\mathbf{r}_{,p}^{\intercal}\delta\mathbf{r}_{,pp}\right) \\ & +EI\frac{2}{|\mathbf{r}_{,p}|^6}\left(\mathbf{r}_{,p}^{\intercal}\mathbf{r}_{,pp}\right)^2\mathbf{r}_{,p}^{\intercal}\delta\mathbf{r}_{,p}\Big]\,dp\end{aligned} \tag{73}$$

By substituting $\mathbf{r}=\mathbf{S}\mathbf{u}$ into above equation, one obtains the expression of δW_S in the form of element coordinates, and it reads

$$\begin{aligned}\delta W_S = & \mathbf{u}^{\intercal}\int_0^L \Big\{ EI\gamma^2\mathbf{S}_{,pp}^{\intercal}\mathbf{S}_{,pp} \\ & -EI\gamma^4\left(\mathbf{S}_{,p}^{\intercal}\mathbf{S}_{,p}\right)\mathbf{u}\mathbf{u}^{\intercal}\left(\mathbf{S}_{,pp}^{\intercal}\mathbf{S}_{,pp}\right)^{\intercal} \\ & -EI\gamma^4\left[\left(\mathbf{S}_{,pp}^{\intercal}\mathbf{S}_{,p}\right)^{\intercal}+\mathbf{S}_{,pp}^{\intercal}\mathbf{S}_{,p}\right]\mathbf{u}\mathbf{u}^{\intercal}\left(\mathbf{S}_{,pp}^{\intercal}\mathbf{S}_{,p}\right) \\ & +2EI\gamma^6\left(\mathbf{u}^{\intercal}\mathbf{S}_{,p}^{\intercal}\mathbf{S}_{,pp}\mathbf{u}\right)^2\mathbf{S}_{,p}^{\intercal}\mathbf{S}_{,p} \\ & +EA(1-\gamma)\mathbf{S}_{,p}^{\intercal}\mathbf{S}_{,p}\Big\}^{\intercal}\,dp\delta\mathbf{u}\end{aligned} \tag{74}$$

where $\gamma=\frac{1}{|\mathbf{r}_{,p}|}$. To make the element computationally more efficient for the cases where the axial deformation of the beam is very small, the γ is approximated as

$$\gamma^n \approx n+1-n|\mathbf{r}_{,p}| = n+1-n\sqrt{(\mathbf{S}_{,p}\mathbf{u})^{\intercal}(\mathbf{S}_{,p}\mathbf{u})} \tag{75}$$

From Eq. (74), the stiffness matrix $\mathbf{K}_s^e$ of the beam element is derived as

$$\begin{aligned}\mathbf{K}_s^e = \int_0^L \Big\{ & EI\gamma^2\mathbf{S}_{,pp}^{\intercal}\mathbf{S}_{,pp} \\ & -EI\gamma^4\left(\mathbf{S}_{,p}^{\intercal}\mathbf{S}_{,p}\right)\mathbf{u}\mathbf{u}^{\intercal}\left(\mathbf{S}_{,pp}^{\intercal}\mathbf{S}_{,pp}\right)^{\intercal} \\ & -EI\gamma^4\left[\left(\mathbf{S}_{,pp}^{\intercal}\mathbf{S}_{,p}\right)^{\intercal}+\mathbf{S}_{,pp}^{\intercal}\mathbf{S}_{,p}\right]\mathbf{u}\mathbf{u}^{\intercal}\left(\mathbf{S}_{,pp}^{\intercal}\mathbf{S}_{,p}\right) \\ & +2EI\gamma^6\left(\mathbf{u}^{\intercal}\mathbf{S}_{,p}^{\intercal}\mathbf{S}_{,pp}\mathbf{u}\right)^2\mathbf{S}_{,p}^{\intercal}\mathbf{S}_{,p} \\ & +EA(1-\gamma)\mathbf{S}_{,p}^{\intercal}\mathbf{S}_{,p}\Big\}\,dp\delta\mathbf{u}.\end{aligned} \tag{76}$$

To make the expression of the stiffness matrix brief, we denote

$$Q_1 = \mathbf{S}_{,pp}^{\intercal}\mathbf{S}_{,pp}, \quad Q_2 = \mathbf{S}_{,pp}^{\intercal}\mathbf{S}_{,p} \quad and \quad Q_3 = \mathbf{S}_{,p}^{\intercal}\mathbf{S}_{,p} \tag{77}$$

Then, the expression of the stiffness matrix of the beam element becomes

$$\begin{aligned}\mathbf{K}_s^e = \int_0^L \Big(& EI\gamma^2 Q_1 - EI\gamma^4 Q_3\mathbf{u}\mathbf{u}^{\intercal}Q_1 \\ & -EI\gamma^4\left(Q_2^{\intercal}+Q_2\right)\mathbf{u}\mathbf{u}^{\intercal}Q_2 \\ & +2EI\gamma^6\left(\mathbf{u}^{\intercal}Q_2^{\intercal}\mathbf{u}\right)^2 Q_3 + EA(1-\gamma)Q_3\Big)\,dp\end{aligned} \tag{78}$$

From Eq.(78), it can be seen that it would not be possible to factorise the element coordinates vector $\mathbf{u}$ out of the integrals because of the presence of γ. Therefore, here, the integrals in Eq.(78) are approximated using a Gaussian quadrature with three integration points.

The last term of Eq.(78), namely $EA(1-\gamma)Q_3$, can be replaced by $\left(EA(1-\gamma)+\gamma\left(P_eA_e-P_iA_i\right)\right)Q_3$ if the effective tension is taken into account. Here, P_e and P_i are the external and internal fluid pressures, which, in offshore applications, usually depend on the depth of the water and are therefore functions of the position vector. The above-mentioned term will be treated separately in different cases with a specific definition of the water depth.

solving algebraic equations Eq.(**??**) and (**??**). However, Eqs.(**??**) and (**??**) are nonlinear, since both the damping and stiffness matrix and the nodal forces are response-dependent, and they need to be solved through iteration. Here, the Newton-Raphson method is applied, and the tangential stiffness (Jacobian matrix) of the system needs to be determined first.

The jacobian matrix of Eqs.(**??**) and (**??**) can be obtained by differentiating them in terms of the element coordinates $\mathbf{u}_{i+1}$ and $\mathbf{q}_{i+1}$. For the sake of simplicity, the subscript $i+1$ is not used in the following derivations. Differentiating Eq.(**??**) with respect to $\mathbf{u}$ gives

$$\mathbf{J}^e_{s,\mathbf{u}} = a_1\mathbf{M}^e_s + b_1\frac{\partial\left(\mathbf{C}^e_s\mathbf{u}\right)}{\partial\mathbf{u}} + \frac{\partial\left(\mathbf{K}^e_s\mathbf{u}\right)}{\partial\mathbf{u}} - \frac{\partial\mathbf{F}^e}{\partial\mathbf{u}} \tag{86}$$

Differentiating Eq. (**??**) respect to $\mathbf{q}$ yields

$$\mathbf{J}^e_{s,\mathbf{q}} = -\frac{\partial\mathbf{F}^e}{\partial\mathbf{q}} \tag{87}$$

Similarly, differentiating Eq. (**??**) respect to $\mathbf{u}$ and $\mathbf{q}$ yields

$$\mathbf{J}^e_{q,\mathbf{u}} = \frac{\partial\left(\mathbf{K}^e_q\mathbf{q}\right)}{\partial\mathbf{u}} - \frac{\partial\mathbf{R}^e}{\partial\mathbf{u}} \tag{88}$$

$$\mathbf{J}^e_{q,\mathbf{q}} = a_1\mathbf{M}^e_q + b_1\frac{\partial\left(\mathbf{C}^e_q\dot{\mathbf{q}}\right)}{\partial\mathbf{q}} + \mathbf{K}^e_q \tag{89}$$

Rayleigh damping has been applied to the structure, and from Eq. (43) it can be derived that

$$\frac{\partial\left(\mathbf{C}^e_s\mathbf{u}\right)}{\partial\mathbf{u}} = \alpha\mathbf{M}^e_s + \beta\mathbf{J}^{e,eq}_s \tag{90}$$

With the expression of beam stiffness matrix given by Eq. (78), it can be derived that

$$\begin{aligned}\frac{\partial\left(\mathbf{K}^e_s\mathbf{u}\right)}{\partial\mathbf{u}} = \int_0^L EI\Big(&\gamma^2Q_1 - 2\gamma^4Q_1\mathbf{u}\mathbf{u}^\intercal Q_3\\ &-\gamma^4\left(\left(\mathbf{u}^\intercal Q_1\mathbf{u}\right)Q_3 + Q_3\mathbf{u}\mathbf{u}^\intercal\left(Q_1+Q_1^\intercal\right)\right) + 4\gamma^6Q_3\mathbf{u}\mathbf{u}^\intercal Q_1\mathbf{u}\mathbf{u}^\intercal Q_3\\ &-\gamma^4\left(\left(\mathbf{u}^\intercal Q_2\mathbf{u}\right)\left(Q_2+Q_2^\intercal\right) + \left(Q_2+Q_2^\intercal\right)\mathbf{u}\mathbf{u}^\intercal\left(Q_2+Q_2^\intercal\right)\right) + 4\gamma^6\left(Q_2+Q_2^\intercal\right)\mathbf{u}\mathbf{u}^\intercal Q_2\mathbf{u}\mathbf{u}^\intercal Q_3\\ &+2\gamma^6\Big(2Q_3\mathbf{u}\mathbf{u}^\intercal Q_2^\intercal\mathbf{u}\mathbf{u}^\intercal\left(Q_2+Q_2^\intercal\right) + \left(\mathbf{u}^\intercal Q_2^\intercal\mathbf{u}\right)^2Q_3\Big) - 12\gamma^8\left(\mathbf{u}^\intercal Q_2^\intercal\mathbf{u}\right)^2Q_3\mathbf{u}\mathbf{u}^\intercal Q_3\Big)\\ &+EA\left(\left(1-\gamma\right)Q_3 + \gamma^3Q_3\mathbf{u}\mathbf{u}^\intercal Q_3\right)dp\end{aligned} \tag{91}$$

As to the external nodal hydrodynamic forces $\mathbf{F}^e$, its derivative respect to $\mathbf{u}$ reads

$$\begin{aligned}\frac{\partial\mathbf{F}^e}{\partial\mathbf{u}} =& \frac{1}{2}\rho D\frac{C_{L0}}{2}\int_0^L\mathbf{S}^\intercal\left(\mathbf{S}_q\mathbf{q}\right)\left(2\mathbf{D}_{VL}\mathbf{U}_N^\intercal\frac{\partial\mathbf{U}_N}{\partial\mathbf{u}} + |\mathbf{U}_N|^2\frac{\partial\mathbf{D}_{VL}}{\partial\mathbf{u}}\right)dp\\ &+\frac{1}{2}\rho DC_{D0}\int_0^L\mathbf{S}^\intercal\left(|\mathbf{U}_N|\mathbf{I} + \frac{\mathbf{U}_N\mathbf{U}_N^\intercal}{|\mathbf{U}_N|}\right)\frac{\partial\mathbf{U}_N}{\partial\mathbf{u}}dp\\ &+\frac{1}{2}\rho D\alpha\frac{C_{L0}^2}{4}\int_0^L\left(\mathbf{S}_q\mathbf{q}\right)^2\mathbf{S}^\intercal\left(\frac{\mathbf{U}_{NX}\mathbf{U}_{NX}^\intercal}{|\mathbf{U}_{NX}|} + |\mathbf{U}_{NX}|\mathbf{I}\right)\frac{\partial\mathbf{U}_{NX}}{\partial\mathbf{u}}dp\end{aligned} \tag{92}$$

where

$$\frac{\partial \mathbf{U}_N}{\partial \mathbf{u}} = b_1 \left[\mathbf{t}^{eq} \left(\mathbf{t}^{eq}\right)^\intercal - \mathbf{I}\right] \mathbf{S} \tag{93}$$

$$\begin{aligned}\frac{\partial \mathbf{D}_{VL}}{\partial \mathbf{u}} =& b_1 \left[\frac{\mathbf{I}}{|\mathbf{t}^{eq} \times \mathbf{U}_N|} - \frac{\left(\mathbf{t}^{eq} \times \mathbf{U}_N\right)\left(\mathbf{t}^{eq} \times \mathbf{U}_N\right)^\intercal}{|\mathbf{t}^{eq} \times \mathbf{U}_N|^3}\right] \\ & \left[\mathbf{t}^{eq}\right]_\times \left[\mathbf{t}^{eq} \left(\mathbf{t}^{eq}\right)^\intercal - \mathbf{I}\right] \mathbf{S}\end{aligned} \tag{94}$$

$$\frac{\partial \mathbf{U}_{NX}}{\partial \mathbf{u}} = -b_1 \mathbf{n}^{eq} \left(\mathbf{n}^{eq}\right)^\intercal \mathbf{S} \tag{95}$$

In Eq. (94), the operator $[]_\times$ denotes the skew -symmetric matrix, which is normally used to represent the cross products as matrix multiplications.

The derivative of $\mathbf{F}^e$ with respect to $\mathbf{q}$ reads

$$\begin{aligned}\frac{\partial \mathbf{F}^e}{\partial \mathbf{q}} =& \frac{1}{2}\rho D \frac{C_{L0}}{2} \int_0^L \mathbf{S}^\intercal |\mathbf{U}_N|^2 \mathbf{D}_{VL} \mathbf{S}_q dp \\ & + \frac{1}{2}\rho D \alpha \frac{C_{L0}^2}{4} \int_0^L 2\left(\mathbf{S}_q \mathbf{q}\right) |\mathbf{U}_{NX}| \mathbf{S}^\intercal \mathbf{U}_{NX} \mathbf{S}_q dp\end{aligned} \tag{96}$$

From Eq. (48), it can be derived that

$$\frac{\partial \left(\mathbf{K}_q^e \mathbf{q}\right)}{\partial \mathbf{u}} = a_1 \frac{\kappa}{D} \int_0^L \mathbf{S}_q^\intercal \mathbf{S}_q \mathbf{q} \left(\mathbf{n}^{eq}\right)^\intercal \mathbf{S} dp \tag{97}$$

Similarly, from Eqs.(53) and (47), the following is obtained.

$$\frac{\partial \mathbf{R}^e}{\partial \mathbf{u}} = \frac{A}{D} \int_0^L \mathbf{S}_q^\intercal \left(\mathbf{b}^{eq}\right) \mathbf{S} dp \tag{98}$$

$$\frac{\partial \mathbf{C}_q^e \dot{\mathbf{q}}}{\partial \mathbf{q}} = 4\pi \mathrm{St}/D \int_0^L |\mathbf{V}_N^{eq}| \left(\mathbf{S}_q \mathbf{q}\right) \left(\mathbf{S}_q \dot{\mathbf{q}}\right) \mathbf{S}_q^\intercal \mathbf{S}_q dp + b_1 \mathbf{C}_q^e \tag{99}$$

B.3 Static example, Cantilever beam

The static problem of the large deformation of a cantilever beam subjected to a tip load, as illustrated in Fig.16, has already been used in literature for comparison, and the iterative solutions by means of the extensible elastic theory are given in [43].

The parameters of the beam consist of length $L = 2$ m, the equivalent bending stiffness $EI = 1.725 \times 10^6$ N/m^2 and the equivalent axial stiffness $EA = 2.07 \times 10^9$ N. The tip load has been chosen according to $F_0 = 3EI/L^2$, which leads to a large deformation. Displacements of the tip in X and Y directions, obtained with different numbers of elements, are presented in Table 2 wherein they are compared with the classical extensible elastic solution given in [43]. The proposed model, with 128 elements, already generates a result that matches the extensible elastic solution up to six digits.

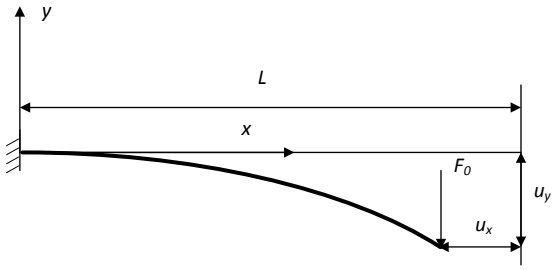

Fig. 16: Cantilever beam subjected to tip load.

Table 2: Axial and transverse displacement of the tip of the cantilever beam using the proposed beam element model and comparison to the analytical solution of the extensible elastica

Elements	u_x	u_y
4	0.509715120993764	1.209144995093078
8	0.508604452895885	1.207351964767034
16	0.508541687577717	1.207246521801250
32	0.508537806636057	1.207240038638574
64	0.508537557824162	1.207239635075415
128	0.508537541233588	1.207239609883485
Ext. elastica	0.508537304325877	1.207239854549824

B.4 Dynamic example, large deformation pendulum

The goal of the second example is to evaluate the performance of the proposed model in the case of 3D motion with a large rotation. The initially straight pendulum that is parallel to the X-Z plane has an initial angular velocity of 4 rad/s about the Y axis. Under the effect of gravity, the flexible pendulum will undergo a large rotation as well as deformation. The parameters of the pendulum consist of length $L = 1$ m, the equivalent bending stiffness $EI = 8.3 \times 10^{-5}$ N/m^2, equivalent axial stiffness $EA = 40$ N and the mass $m = 0.008$ kg/m. With only four elements, the implicit Newmark-beta method as described in **??** is used to calculate the response of the pendulum with time steps of 0.1 ms. Fig.17(a) illustrates the position of the tip projected in X-Z plane, and Fig.C.2(b) shows the Y position of the middle point of the pendulum. A comparison are made between the solution of the proposed model and the cable element in [31]. Both figures indicate that the proposed model performs well in the case of 3D motion with a large rotation.

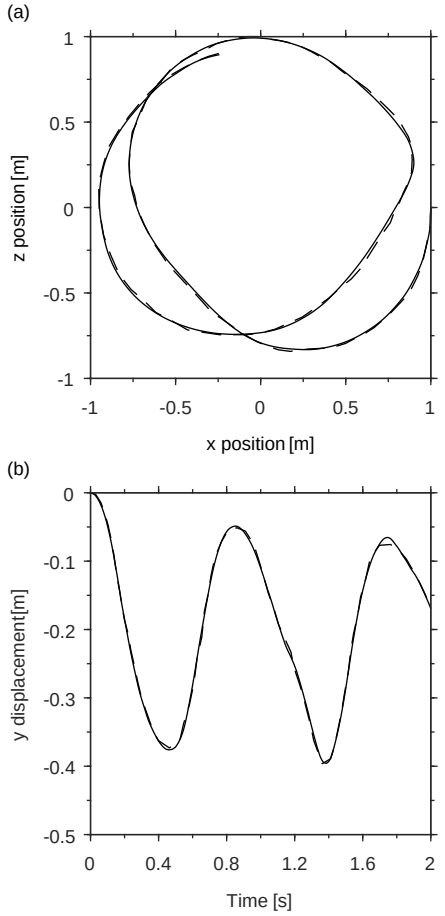

Fig. 17: Dynamic response of a large deformation pendulum. (a) Plot of the Z versus X co-ordinate of the mid-point of the three-dimensional pendulum; (b) Y-displacement of the mid-point of the three-dimensional pendulum as function of time. Simulation results with the proposed model are represented by dashed lines and reference results are represented by solid lines.

References

1. Qu, Y., Metrikine, A.: A single van der Pol wake oscillator model for coupled cross-flow and in-line vortex-induced vibrations. Ocean Engineering. 196, 106732 (2020)
2. Violette, R., de Langre, E., Szydlowski, J.: Computation of vortex-induced vibrations of long structures using a wake oscillator model: Comparison with DNS and experiments. Computers and Structures. 85(11), 1134-1141 (2007)
3. Ge, F., Long, X., Wang, L., Hong, Y.: Flow-induced vibrations of long circular cylinders modeled by coupled nonlinear oscillators. Science in China Series G: Physics, Mechanics and Astronomy. 52(7), 1086-1093 (2009)
4. Sun, L., Zong, Z., Dong, J., Dong, G.H., Liu, C.F.: Strip-wise discrete vortex method for VIV analysis of flexible risers. Journal of Fluids and Structures. 35, 21-49 (2012)
5. Bai, X., Qin, W.: Using vortex strength wake oscillator in modelling of vortex induced vibrations in two degrees of freedom. European Journal of Mechanics - B/Fluids. 48, 165-173 (2014)
6. Srinil, N., Wiercigroch, M., O'Brien, P.: Reduced-order modelling of vortex-induced vibration of catenary riser. Ocean Engineering. 36, 1404-1414 (2009)
7. Srinil, N.: Multi-mode interactions in vortex-induced vibrations of flexible curved/straight structures with geometric nonlinearities. Journal of Fluids and Structures. 26, 1098-1122 (2010)
8. Zanganeha, H., Srinil, N.: Three-dimensional VIV prediction model for a long flexible cylinder with axial dynamics and mean drag magnifications. Ocean Engineering. 66, 127-146 (2016)
9. Sarpkaya, T.: Fluid forces on oscillating cylinders. NASA STI/Recon Technical Report A. 78, 275-290 (1978)
10. Gopalkrishnan, R.: Vortex-induced forces on oscillating bluff cylinders. PhD thesis, Woods Hole Oceanographic Inst., MA (1993)
11. Hover, F.S., Techet, A.H., Triantafyllou, M.S.: Forces on oscillating uniform and tapered cylinders in crossflow. J. Fluid Mech. 363, 97-114 (1998)
12. Morse, T.L., Williamson, C.H.K.: Fluid forcing, wake modes, and transitions for a cylinder undergoing controlled oscillations. Journal of Fluids and Structures. 25, 697-712 (2009)
13. Lu, Z., Fu, S., Zhang, M., Ren, H., Song, L.: A modal space based direct method for vortex-induced vibration prediction of flexible risers. Ocean Engineering. 152, 191-202 (2018)
14. Dahl, J.M.: Vortex-induced vibration of a circular cylinder with combined in-line and cross-flow motion. PhD thesis, Massachusetts Institute of Technology, MA (2008)
15. Gabbai, R.D., Benaroya, H.: An overview of modeling and experiments of vortex-induced vibration of circular cylinders. Journal of Sound and Vibration. 282, 575-616 (2005)
16. Nayfeh, A., Owis, F., Hajj, M.: A Model for the Coupled Lift and Drag on a Circular Cylinder. In DETC2003/VIB, 1289-1296 (2003)
17. Facchinetti, M., de Langre, E., and Biolley, F.: Coupling of structure and wake oscillators in vortex-induced vibrations. Journal of Fluids and Structures. 19, 123-140 (2004)
18. Ogink, R., Metrikine, A.: A wake oscillator with frequency dependent coupling for the modeling of vortex-induced vibration. Journal of Sound and Vibration. 329, 5452-5473 (2010)
19. Mottaghi, S., Benaroya, H.: Reduced-order modeling of fluid-structure interaction and vortex-induced vibration systems using an extension of Jourdain's principle. Journal of Sound and Vibration. 382, 193-212 (2016)
20. Gabbai, R.D., Benaroya, H.: A first-principles derivation procedure for wake-body models in vortex-induced vibration: Proof-of-concept. Journal of Sound and Vibration. 312(1), 19-38 (2008)
21. Thorsen, M., Sævik, S., Larsen, C.: A simplified method for time domain simulation of cross-flow vortex-induced vibrations. Journal of Fluids and Structures. 49, 135-148 (2014)
22. Zhang, M., Fu, S., Song, L., Tang, X., He, Y.: A time domain prediction method for the vortex-induced vibrations of a flexible riser. Marine Structures. 59, 458-481 (2018)
23. Lu, Z., Fu, S., Zhang M., Ren, H.: An efficient time-domain prediction model for vortex-induced vibration of flexible risers under unsteady flows. Marine Structures. 64, 492-519 (2019)

24. Jauvtis, N., Williamson, C.H.K.: The effect of two degrees of freedom on vortex-induced vibration at low mass and damping. Journal of Fluid Mechanics. 509, 23-62 (2004)
25. Dahl, J.M., Hover, F.S., Triantafyllou, M.S., Dong, S., Karniadakis, G.E.: Resonant vibrations of bluff bodies cause multivortex shedding and high frequency forces. Physical review letters. 99(14), 144503 (2007)
26. Aronsen, K. H.: An Experimental Investigation of In-line and Combined In-line and Cross-flow Vortex Induced Vibrations. PhD thesis, Norwegian University of Science and Technology, Trondheim (2007)
27. Kim, W.-J., Perkins, N.: Two-dimensional vortex-induced vibration of cable suspensions. Journal of Fluids and Structures. 16(2), 229-245 (2002)
28. Srinil, N., Zanganeh, H.: Modelling of coupled cross-flow/in-line vortex-induced vibrations using double duffing and van der pol oscillators. Ocean Engineering. 53, 83-97 (2012)
29. Postnikov, A., Pavlovskaia, E., Wiercigroch, M.: 2DOF CFD calibrated wake oscillator model to investigate vortex-induced vibrations. International Journal of Mechanical Sciences. 127, 176-190 (2017)
30. Chaplin, J.R., Bearman, P.W., Huera-Huarte, F.J., Pattenden, R.: Laboratory measurements of vortex-induced vibrations of a vertical tension riser in a stepped current. Journal of Fluids and Structures. 21(1), 3-24 (2005)
31. Gerstmayr, J., Shabana, A.A.: Analysis of thin beams and cables using the absolute nodal co-ordinate formulation. Nonlinear Dynamics. 45(1), 109-130 (2006)
32. Géradin, M., Cardona, A.: Flexible Multibody Dynamics: A Finite Element Approach. Wiley, New York (2001)
33. Qin, L.: Development of Reduced-Order Models for Lift and Drag on Oscillating Cylinders with Higher-Order Spectral Moments. PhD thesis, Virginia Polytechnic Institute and State University, VA (2004)
34. Wang, E., Xiao, Q.: Numerical simulation of vortex-induced vibration of a vertical riser in uniform and linearly sheared currents. Ocean Engineering. 121, 492-515 (2016)
35. Dahl, J., Hover, F., Triantafyllou, M.: Two-degree-of-freedom vortex-induced vibrations using a force assisted apparatus. Journal of Fluids and Structures. 22(6), 807-818 (2006)
36. O'Neill, B.: Elementary Differential Geometry. Academic Press, Boston, revised second edition (2006).
37. Huera Huarte, F.J.: Multi-mode vortex-induced vibrations of a flexible circular cylinder. PhD Thesis, Imperial College London, London (2006).
38. Lie, H., Kaasen, K.E.: Modal analysis of measurements from a large-scale VIV model test of a riser in linearly sheared flow. Journal of Fluids and Structures. 22(4), 557-575 (2006)
39. Mina, A.: Modeling the vortex-induced vibrations of a multi-span free standing riser. Master Thesis, Delft University of Technology, Delft (2013)
40. Kallias Ntroumpis, D.F.: VIV analysis of a subsea power cable during installation in high current seas. Master Thesis, Delft University of Technology, Delft (2017)
41. Mukundan, H.: Vortex-induced Vibration of Marine Risers: Motion and Force Reconstruction from Field and Experimental Data. PhD Thesis, Massachusetts Institute of Technology, MA (2008).
42. Seyed-Aghazadeh, B., Modarres-Sadeghi, Y.: Reconstructing the vortex-induced-vibration response of flexible cylinders using limited localized measurement points. Journal of Fluids and Structures. 65, 433-446 (2016)
43. Gerstmayr, J., Irschik, H.: On the correct representation of bending and axial deformation in the absolute nodal coordinate formulation with an elastic line approach. Journal of Sound and Vibration. 318(3), 461-487 (2008)